

## RESEARCH ARTICLE

# Strength-dependent perturbation of whole-brain model working in different regimes reveals the role of fluctuations in brain dynamics

Yonatan Sanz Perl <sup>1,2,3\*</sup>, Anira Escrichs <sup>1</sup>, Enzo Tagliazucchi <sup>2,4</sup>, Morten L. Kringelbach <sup>5,6,7</sup>\*, Gustavo Deco <sup>1,8,9,10</sup>\*

**1** Center for Brain and Cognition, Computational Neuroscience Group, Department of Information and Communication Technologies, Universitat Pompeu Fabra, Barcelona, Spain, **2** Department of Physics, University of Buenos Aires, Buenos Aires, Argentina, **3** Cognitive Neuroscience Center, Universidad de San Andrés, Buenos Aires, Argentina, **4** Latin American Brain Health Institute (BrainLat), Universidad Adolfo Ibáñez, Santiago, Chile, **5** Centre for Eudaimonia and Human Flourishing, Linacre College, University of Oxford, Oxford, United Kingdom, **6** Department of Psychiatry, University of Oxford, Oxford, United Kingdom, **7** Center for Music in the Brain, Department of Clinical Medicine, Aarhus University, Denmark, **8** Institució Catalana de la Recerca i Estudis Avançats (ICREA), Barcelona, Spain, **9** Department of Neuropsychology, Max Planck Institute for Human Cognitive and Brain Sciences, Leipzig, Germany, **10** School of Psychological Sciences, Monash University, Melbourne, Clayton Victoria Australia

\* These authors contributed equally to this work.

\* [yonatan.sanz@upf.edu](mailto:yonatan.sanz@upf.edu) (YSP); [morten.kringelbach@psych.ox.ac.uk](mailto:morten.kringelbach@psych.ox.ac.uk) (MK); [gustavo.deco@upf.edu](mailto:gustavo.deco@upf.edu) (GD).



## OPEN ACCESS

**Citation:** Sanz Perl Y, Escrichs A, Tagliazucchi E, Kringelbach ML, Deco G (2022) Strength-dependent perturbation of whole-brain model working in different regimes reveals the role of fluctuations in brain dynamics. *PLoS Comput Biol* 18(11): e1010662. <https://doi.org/10.1371/journal.pcbi.1010662>

**Editor:** Jean Daunizeau, Brain and Spine Institute (ICM), FRANCE

**Received:** February 15, 2022

**Accepted:** October 17, 2022

**Published:** November 2, 2022

**Copyright:** © 2022 Sanz Perl et al. This is an open access article distributed under the terms of the [Creative Commons Attribution License](https://creativecommons.org/licenses/by/4.0/), which permits unrestricted use, distribution, and reproduction in any medium, provided the original author and source are credited.

**Data Availability Statement:** All code written in support of this publication is publicly available at [https://github.com/yonisanzperl/on\\_the\\_edge](https://github.com/yonisanzperl/on_the_edge). The data is publicly available on <https://www.humanconnectome.org/study/hcp-young-adult>.

**Funding:** Y.S.P, A.E and G.D are funded by HBP SGA3 Human Brain Project Specific Grant Agreement 3 (grant agreement no. 945539), funded by the EU H2020 FET Flagship programme (<https://research-and-innovation.ec.europa.eu/>)

## Abstract

Despite decades of research, there is still a lack of understanding of the role and generating mechanisms of the ubiquitous fluctuations and oscillations found in recordings of brain dynamics. Here, we used whole-brain computational models capable of presenting different dynamical regimes to reproduce empirical data's turbulence level. We showed that the model's fluctuations regime fitted to turbulence more faithfully reproduces the empirical functional connectivity compared to oscillatory and noise regimes. By applying global and local strength-dependent perturbations and subsequently measuring the responsiveness of the model, we revealed each regime's computational capacity demonstrating that brain dynamics is shifted towards fluctuations to provide much-needed flexibility. Importantly, fluctuation regime stimulation in a brain region within a given resting state network modulates that network, aligned with previous empirical and computational studies. Furthermore, this framework generates specific, testable empirical predictions for human stimulation studies using strength-dependent rather than constant perturbation. Overall, the whole-brain models fitted to the level of empirical turbulence together with functional connectivity unveil that the fluctuation regime best captures empirical data, and the strength-dependent perturbative framework demonstrates how this regime provides maximal flexibility to the human brain.

[funding/funding-opportunities/funding-programmes-and-open-calls/horizon-2020\\_en](#))

The funders had no role in study design, data collection and analysis, decision to publish, or preparation of the manuscript.

**Competing interests:** The authors have declared that no competing interests exist.

## Author summary

How and why do complex, fluctuating, and oscillating dynamics characterise brain states? We combined a whole-brain model and strength-dependent perturbation frameworks to investigate the causal mechanistic explanation behind the human brain function. We demonstrated by fitting whole-brain models to the level of empirical turbulence together with functional connectivity that the fluctuation regime best captures empirical data. Furthermore, the strength-dependent perturbative approach allows us to assess the computational capabilities of different dynamical regimes. We showed that the fluctuations regime provides maximal flexibility to the human brain, a desirable property for brain dynamics to interact with the environment.

## Introduction

Already at the birth of neuroscience, a deep problem emerged: namely that local and global recordings from inside and outside the brain show very complex fluctuating and oscillating patterns of brain activity [1–5]. This gave rise to the fundamental question of the importance of synchronous or asynchronous local dynamics as the origin of the dynamical behaviour of brain states [6,7]. In global brain dynamics, a purely fluctuating scenario will give rises to patterns formed due to noise correlations, whereas a purely oscillatory regime would produce patterns arising mainly from cluster synchronisation. In both cases, the activity is shaped by the underlying brain anatomy but the generating principles are clearly different. Even more, the asynchronous, irregular background dynamics have been associated with conscious, responsive brain state, while synchronisation and regular dynamics have been linked with reduced states of conscious awareness [6].

Deco & Kringelbach have proposed a novel framework based on recent results showing turbulence in the brain dynamics, which is based on quantifying the level of local synchronisation in whole-brain activity [8–10]. Briefly, turbulence dynamics in non-fluid systems can be defined by the coupled oscillator framework of Kuramoto [11,12]. In this sense, brain dynamics present turbulent behaviour regarding the amplitude variability of the local Kuramoto order parameter. Furthermore, turbulence has been shown to provide the optimal transmission of energy (which is closely related to information [13]), and at the core of this transmission are the scale-free mixing properties of turbulence. Kolmogorov's seminal phenomenological statistical studies have shown that this transmission is highly efficient across scales within the turbulent regime [14,15]. In Deco & Kringelbach approach, it has also been shown that this efficient transmission, which is demonstrated in power laws relation between information and space, is also present in brain dynamics [8]. Note that for these power laws, the flow is not provided by billions of molecules in a fluid but by the flow of information coming from the interplay and mutual entrainment in billions of neurons underlying brain dynamics.

Further to these empirical observations, the relevance of whole-brain computational model within this analytical framework was demonstrated based on the fact that brain dynamics can be accurately modelled by a system of coupled non-linear Stuart-Landau working in a turbulent regime [8,10], which integrates anatomy and local dynamics [16–19]. As it happens, this whole-brain model is suited to resolve the question in hand, since it naturally describes the transitions between noise, fluctuation and oscillation. The whole-brain system can produce three radically different regimes, simply by varying the local bifurcation parameter: 1) *Noise* regime—when the parameter is much less than zero, 2) fluctuating *subcritical* regime—when the

parameter is just below zero; and 3) oscillatory *supercritical* regime—when the parameter is larger than zero. Previous research has shown that the three different scenarios of noise [20,21], subcritical [16,21–23] and supercritical [24] are equally able to fit the empirical neuro-imaging data in terms of functional connectivity. However, it is not clear when fitting the whole-brain model to the level of turbulence which regimes are able to fit the empirical data.

In a complementary direction, empirical perturbations have proved to be an excellent approach to provide insights into the complexity of brain dynamics, such as the one proposed by Massimini and colleagues. The authors used transcranial magnetic stimulation (TMS) with electroencephalography (EEG) to demonstrate perturbation-elicited changes in global brain activity in the perturbative complexity index (PCI) between different brain states (wakefulness, sleep, anaesthesia and coma) [25–27]. The results showed, for example, that non-REM sleep is accompanied by a breakdown in cortical effective connectivity, where the stimuli rapidly extinguish and do not propagate beyond the stimulation site [25–27]. Based on the same strategy, previous experimental research demonstrated that stimulation with TMS in specific brain regions can differentially modulate specific networks [28,29]. Computational approaches also demonstrated that *constant* perturbation can also provide clear insights into the complexity of brain dynamics (Deco et al., 2018; Goldman et al., 2020; Kunze et al., 2016).

To address the question of distinguishing between noise, fluctuation and oscillations regimes in shaping global brain dynamics, we constructed and perturbed whole-brain models taking advantage of the recently proposed turbulence framework. First, we fitted the model to the level of empirical turbulence to precisely locate the optimal parameters in each regime, showing that the noise regime is suboptimal compared with fluctuations and oscillations that are equally good. To disentangle the generative roles of the fluctuation (subcritical) and oscillations (supercritical) models, we investigated the performance of each model regime in the corresponding optimal working point to fit empirical turbulence at fitting the functional connectivity (probably one of the major outcome measures evaluated thus far in the literature [31,32]). We found that the fluctuations regime overperforms the oscillatory regime showing that the conjunction of turbulence and FC fitting provides the information to unveil the best model regime that captures the empirical observables. We then created a global and local strength-dependent perturbational framework to characterise the computational capabilities in each regime in terms of the responsiveness to external stimulus. To do so, we quantified the evolution of three perturbative sensitivity measures, susceptibility, information capability (defined in the turbulence framework [10]) and the well-known PCI, as a function of the applied global sustained perturbation. The susceptibility is the ability of the system to be externally perturbed, based on the work of Hiroaki Daido [33], who defines the susceptibility of a large population of coupled oscillators as the variation in the system synchronisation under external perturbation. The information capability measures the ability of the system to encode external inputs, as such is closely related to automatic complexity evaluator (ACE), and synchrony coalition entropy (SCE) (used and defined in [34]). We found that the fluctuation regime provides maximal flexibility to brain dynamics, a desirable property for brain dynamics to interact with the environment. The stimulation in the fluctuation regime also provides a mechanistic explanation of experimentally reported brain dynamics showing the modulation of specific resting-state networks when they are perturbed. We show that using a combined whole-brain model fitting and strength-dependent perturbations—instead of the classical flat, constant perturbations—framework provides the means for disentangling alternative model-based hypotheses about the underlying empirical dynamics and characterising their computational capabilities. Our results show that the fluctuation regime more faithfully reproduces empirical properties such as the level of turbulence and functional connectivity, allowing maximal flexibility in information processing.

## Results

In this study, we were interested in revealing the underlying mechanisms of the different dynamical regimes available in the resting state [2,35]. We extended the well established perturbative approach to use strength-dependent, non-constant perturbation in a whole-brain model fitting the empirical data to provide a causal mechanistic explanation for disentangling fluctuating from oscillating regimes in the underlying empirical dynamics. Fig 1 shows the details of our framework, which has two key ingredients: 1) a *model-based* approach which is probed with 2) varying levels of *strength-dependent perturbations*. The whole-brain model is based on the recent of demonstrating turbulence (Fig 1A) in empirical neuroimaging data (Fig 1B). Turbulence is a property found in high-dimensional non-linear systems, where its mixing capability is crucial for giving rise to the efficient energy/information cascade, whereby large whirls turns into smaller whirls and eventually energy dissipation. Using this turbulence framework, we were able to determine the vorticity, i.e. the local level of synchronisation, allowing us to extend the standard global time-based measure of metastability to become a local-based measure of both space and time for capturing the essential features of the underlying brain dynamics.

The Hopf whole-brain model can fit the complex spatiotemporal brain dynamics in terms of both functional connectivity and turbulence (Fig 1C). More generally, the Hopf whole-brain model integrates anatomical connections [36–38] with local dynamics to explain and fit the emergence of global dynamics in empirical data [16,32,39–41] (Fig 1D). For decades, brain signals have been recorded with a plethora of different techniques showing them to be combinations of at least three different regimes: noise, fluctuating, and oscillatory. The non-linear Stuart Landau oscillator is perfect for generating and testing these three regimes, given that the local bifurcation parameter in the equation governs the dynamics of each local brain region (Fig 1E). Indeed, by varying this parameter the Stuart-Landau equation will produce three radically different signals: 1) a noise signal resulting from Gaussian noise added to a fixed point when the parameter is much less than zero resulting in a pure noise signal; 2) a fluctuating stochastically structured signal when the parameter is just below zero, which allows the system to fluctuate between noise and oscillations; 3) an oscillatory signal when the parameter is larger than zero. Technically, these three regimes are termed noise, subcritical and supercritical, respectively.

In the following, we show that the subcritical fluctuating and supercritical oscillatory regimes are equally able to fit the empirical data in terms of functional connectivity and turbulence (Fig 1F). Crucially, however, our framework includes the second ingredient of strength-dependent perturbation, which, as shown below, has allowed us to distinguish between the two regimes. We probe the model in two ways using both global (Fig 1G) and local strength-dependent perturbations (Fig 1H) and measuring the sensitivity of the system through quantifying the elicited susceptibility, information capacity and perturbative complexity index.

### Hopf whole-brain model of large-scale empirical neuroimaging data

We first investigated the ability of the three regimes to fit empirical data. We fitted whole-brain models of Stuart Landau oscillators in the three regimes to the large-scale neuroimaging resting state fMRI data from 1003 healthy human participants in the Human Connectome Project (HCP) [42]. We extracted the timeseries in the Schaefer1000 parcellation [43], a fine-grained atlas that allowed quantified turbulence in empirical data [8].

Previous Hopf whole-brain models have successfully fitted functional neuroimaging data with different acquisition parameters from many different neuroimaging setups [32,44,45] using a fluctuating regime with a local bifurcation parameter close to the bifurcation point.

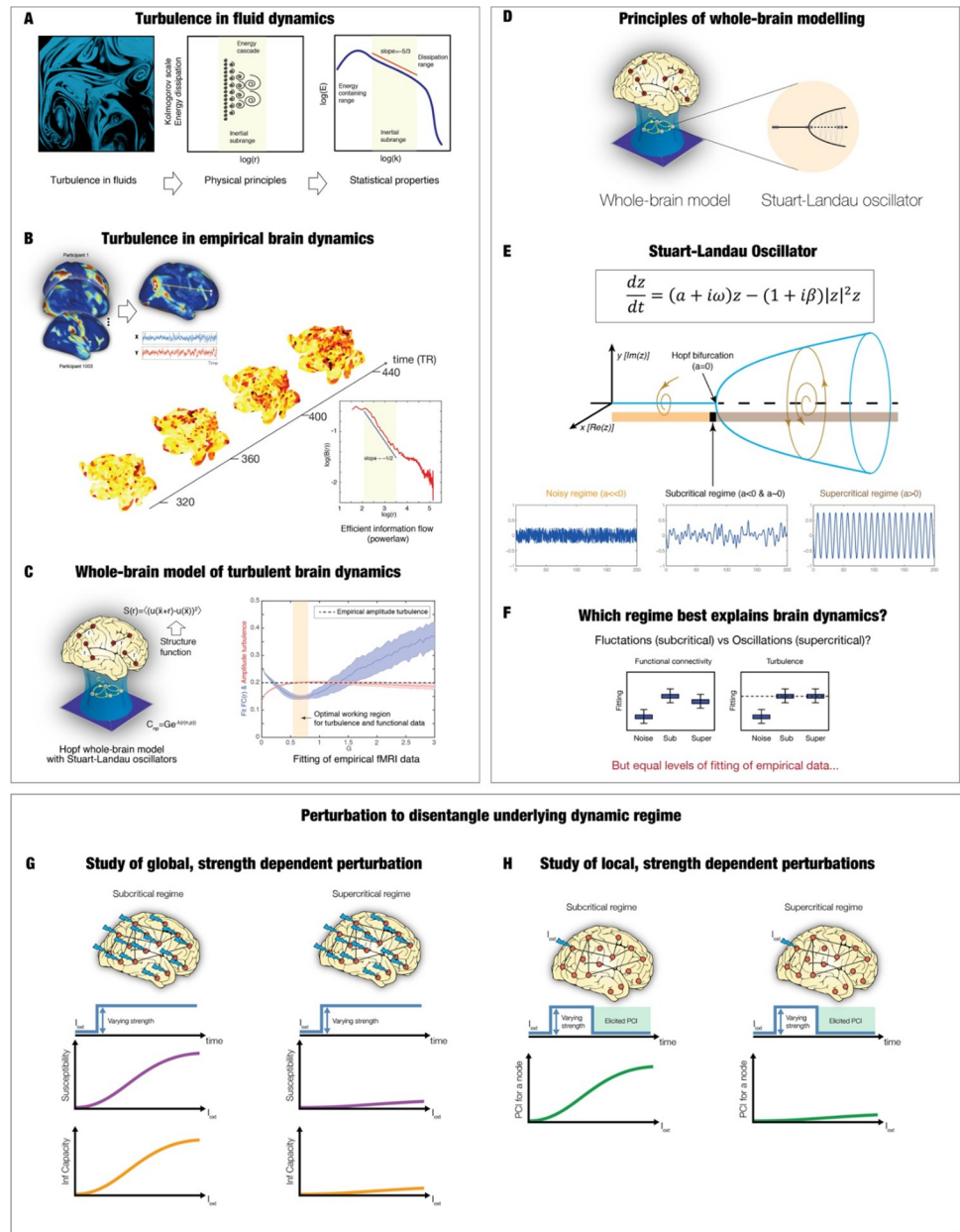


**Fig 1. Overview of the framework.** A) Turbulence provides a good description of the seemingly chaotic dynamics of fluids as first described by Leonardo da Vinci [9] (left panel drawing of turbulent whirls). The physical principles giving rise to turbulence are given by high-dimensional spacetime non-linear coupled systems. In turbulence, a fundamental property is its mixing capability which yields the energy cascade through turning large whirls into smaller whirls and eventually energy dissipation (middle panel). Furthermore, the turbulent energy cascade has been shown to be highly efficient across scales, as evidenced by a power law (right panel). B) Empirical brain dynamics was recently shown to exhibit turbulence [8]. The MRI resting state analysis over 1000 healthy participants (left panel) shows the presence of highly variable, local synchronisation vortices across time and space (middle panel). Equally, the turbulent brain regime also gives rise to an efficient information cascade obeying a power law (right panel). C) Furthermore, Hopf whole-brain models [16] (left panel) were able to fit both turbulence and the empirical data at the same working point (right panel). D) We model brain activity as a system of non-linear Stuart Landau oscillators, coupled by known anatomical connectivity. E) The Stuart Landau equation (top panel) is suited for describing the transitions between noise and oscillation. By varying the local bifurcation parameter,  $a$ , the equation will produce three radically different regimes: Noise ( $a < 0$ ), fluctuating subcritical regime ( $a < 0$  &  $a=0$ ) and oscillatory supercritical regime ( $a > 0$ ) (bottom panel). F) We evaluated the fitting capacity of the three model regimes in terms of functional connectivity and turbulence (with the dashed line showing the empirical level of turbulence). G) However, it is well-known that physical systems can be more deeply probed by perturbing them. Therefore, we used strength-dependent perturbations to

disentangle the generative roles of the fluctuation (subcritical) and oscillations (supercritical) models. We observed the evolution of two key perturbative measures, susceptibility and information capacity, as a function of the applied global sustained perturbation. **H**) Finally, in order to generate experimentally testable hypotheses, we used local strength-dependent, non-sustained perturbations and measured the elicited dynamics in terms of the empirical perturbative complexity index [25]. Specifically, we simulated 600 volumes with the perturbation active, and we then evaluated the evolution of the signals in the following 200 volumes without perturbation and computed the difference between the PCI after and before perturbation.

<https://doi.org/10.1371/journal.pcbi.1010662.g001>

Here we aim to fit both functional connectivity and turbulence of functional neuroimaging data. The functional connectivity defined as the Pearson correlation between all pairs of nodes signal and the turbulence defined as the amplitude variability of the local Kuramoto order parameters. In order to fit turbulence with the Stuart-Landau oscillator in the oscillatory supercritical regime, Kuramoto and colleagues [12] have shown that an extra parameter, the so-called shear parameter, is fundamental. This parameter is also called the “nonisochronicity parameter” and provides a different path to controls the synchronicity of coupled oscillators [13,46,47]. Specifically, this parameter can prevent the full synchronization of oscillators when are coupled [46], which is counterintuitive and necessary to fit brain dynamics. Following the analogy with fluids dynamics this parameter is related with the viscosity of the media [11–13]. Therefore, we extend the Hopf whole-brain model to use the appropriate formulation of the Stuart-Landau equation (see [Methods](#)) to be able to fit the data with the supercritical regime.

We explored the parameter space of varying the global coupling ( $G$ ) and the shear parameter ( $\beta$ ). The coupling parameter ( $G$ ) scales the local fibre densities of the anatomical structural connectivity (see [Methods](#)) to capture the effectivity of the coupling by assuming a single global conductivity parameter. The shear parameter ( $\beta$ ) acts similar to viscosity in fluid dynamics [11] in that it is able to affect both the frequency and amplitude of the generated oscillations [12]. Importantly, for the structural connectivity in the whole-brain model, we used a combination of exponential distance rule, EDR [48] and long-range connections (LR), which improve the fit to the available dMRI tractography from humans [10](see [Methods](#)).

In order to fit the whole-brain model, we used the following observables: 1) the empirical mean level of amplitude turbulence, as the standard deviation of the Kuramoto Local order parameter ( $D$ ), in fine parcellation, and metastability, as the standard deviation of the Kuramoto Global order parameter ( $M$ ), in coarse parcellation; and 2) the grand average functional connectivity (FC) from the neuroimaging empirical data (see [Methods](#)). For measuring the level of fitting for each: 1) for turbulence/metastability measure, we computed the error ( $eD = \text{abs}(D_{\text{sim}} - D_{\text{emp}})$ )/( $eM = \text{abs}(M_{\text{sim}} - M_{\text{emp}})$ ), i.e. by the absolute difference between the simulated and empirical amplitude turbulence and 2) for the functional connectivity, we computed Euclidean distance ( $eFC$ ) between the simulated and empirical FC.

## Modelling results for fine-scale parcellation with 1000 regions

[Fig 2](#) shows the results of fitting the Hopf whole-brain model in the three different regimes (noise, fluctuating and oscillatory, see upper row) for the Schaefer1000 parcellation in terms of functional connectivity and turbulence. For each of these regimes, we defined a grid of the parameter space ( $G, \beta$ ), where  $G$  is the coupling strength factor, i.e. the global scaling factor of regional connectivity and  $\beta$ , the shear parameter (see above and [Methods](#)). For each pair in the grid, the whole-brain dynamics were simulated 100 times, and we computed the level of fitting between amplitude turbulence (second row) and simulated and empirical FC (third row).

We found the optimal fitting for turbulence for each of the three regimes, indicated with a star in the second row of [Fig 2A–2C](#). [Fig 2A](#) shows the best fit for the noise regime ( $a = -1.3$ ) with optimal  $(G, \beta) = (1.8, 0)$  as the absolute difference between the simulated and empirical

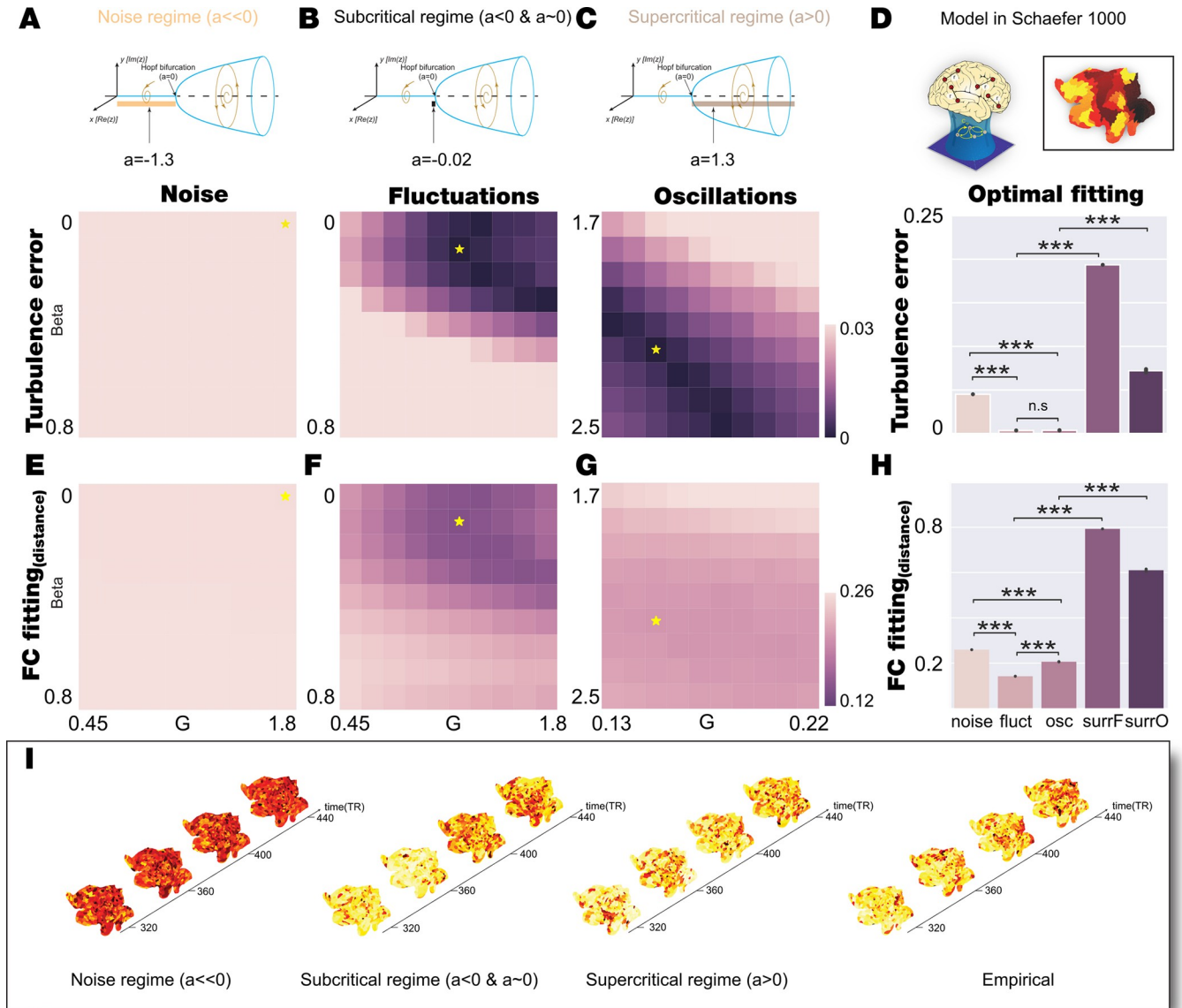


**Fig 2. Model Schaefer1000 fitting of noise, fluctuations, and oscillatory for 1) Turbulence and 2) FC.** A-C) We explored the bi-dimensional parameter space defined by  $\beta$  and  $G$  for noise, fluctuating and oscillatory regime (bifurcation parameter  $a = -1.3$ ,  $a = -0.02$  and  $a = 1.3$ , respectively, indicated in upper row). We computed the level of amplitude turbulence error as the absolute difference between the empirical and simulated turbulence. Yellow stars indicate the  $(\beta, G)$  combination that reaches the lowest turbulence error in each regime. **D**) The upper subpanel shows the model fitting scheme in fine Schaefer1000 parcellation (the render on a flatmap of the hemisphere stands for a scheme of brain regions considered in this parcellation). The bottom subpanel displays the barplot that indicates the statistical distribution of the level of amplitude turbulence obtained by simulating 20 trials with 100 subjects for each model regime with the parameters set at the corresponding working point. We also display the results of two model-based surrogates created by increasing the shear parameter of each model regime. The red dashed line indicates the empirical level of amplitude turbulence averaged across participants. The subcritical, supercritical and empirical level of turbulence are not statistically different (Wilcoxon test,  $P = 0.33$ ), the rest of the comparison are statistically significant (Wilcoxon test,  $P < 0.001$ ). **E-G**) We explored the bi-dimensional parameter space defined by  $\beta$  and  $G$  for noise, fluctuating and oscillatory regime computed the FC fitting as Euclidean distance between the empirical and simulated FC. Yellow stars indicate the  $(\beta, G)$  combination that reaches the lower turbulence error in each regime (the optimal working point obtained in panels A-C). **H**) The barplot indicates the statistical distribution of the FC fitting obtained by simulating 20 trials with 100 subjects for each model regime at the corresponding working point defined as the minimum turbulence error. We also display the results for the model-based surrogates. All comparisons are statistically significant (Wilcoxon,  $P < 0.001$ ). **I**) Visualization of the change of the local Kuramoto order parameter,  $R$ , in space and time reflecting amplitude turbulence in a single simulation at the optimal working point of each regime (noise, fluctuating and oscillatory cases) and one participant (empirical). This can be appreciated from continuous snapshots for segments separated in time rendered on a flatmap of the hemisphere.

<https://doi.org/10.1371/journal.pcbi.1010662.g002>

turbulence  $D$  (here  $eD = 0.0473$ ). **Fig 2B** shows the best fit for the fluctuating regime ( $a = -0.02$ ) with optimal  $(G, \beta) = (1.2, 0.1)$ , which produces a good fit with  $eD = 4 \times 10^{-4}$ . **Fig 2C** shows the best fit for the oscillatory regime ( $a = 1.3$ ) with optimal  $(G, \beta) = (0.15, 2.2)$ , which also produces a good fit with  $eD = 3 \times 10^{-4}$ . We also computed the grid fitting for the FC for all three regimes (**Fig 2E–2G**), with a star in the grid indicating the optimal fit of turbulence which is the criterium for selecting the optimal working point since this is a measure that favours the brain information transmission and its responsiveness [8,10]. Note that these points do not correspond to the optimal fitting with FC in the three regimes. We replicated this analysis by changing the connectivity between non-linear oscillators from the EDR-LR to the structural connectivity (SC) to assess how robust are the results (**S1 Fig**). We found that despite the levels of fitting and parameters space values are modified, both the fluctuating and oscillatory regimes are good for fitting the level of empirical turbulence in the same region of the  $(G, \beta)$  parameter space.

In summary, both the fluctuating and oscillatory regimes are good for fitting the turbulence in the empirical data, while the noise regime is not. This is quantified in **Fig 2D**, which shows the statistical comparisons between optimal fitting (indicated with the stars in **Fig 2A–2C**) of the three regimes with turbulence (repeated 20 times 100 simulations) and a horizontal line of  $D = 0.1976$  indicates the level of empirical turbulence.

The results show that the best working point for the noise regime is only giving mean  $D = 0.1484$ , which is significantly worse than both fluctuating and oscillatory regimes (Wilcoxon  $p < 0.001$ , compare noise and fluctuation; Wilcoxon  $p < 0.001$ , compare noise with oscillatory in **Fig 2D**). On the other hand, the fluctuating and oscillatory regimes are good at fitting the data (mean  $D = 0.1972$  and mean  $D = 0.1973$  respectively) but not significantly different (Wilcoxon  $P = 0.33$ , comparing second with the third bar in **Fig 2D**).

Further bolstering these findings, we also generated model-surrogates (see **Methods**) to compare with the corresponding optimal working point by setting the parameters of the model in the optimal working point but increasing  $\beta$ , which is known to suppress turbulence [8]. Hence, we produced two surrogate models: *surr\_fluct* for the fluctuating model surrogates using  $a = -0.02$  and  $(G, \beta) = (1.2, 6)$  and *surr\_osc* for the oscillatory model surrogates using  $a = 1.3$  and  $(G, \beta) = (0.15, 6)$ . The results clearly show significant differences comparing with the level of turbulence fitting obtained by the optimal working point of the model in different regimes (Wilcoxon  $p < 0.001$ , comparing fluctuation with *surr\_fluct* and comparing oscillations with *surr\_osc*).

Similarly, we fitted the whole-brain model with the functional connectivity by means of the Euclidean distance with the empirical. In **Fig 2E–2G**, we show the fitting for  $(G, \beta)$  for the noise, fluctuating and oscillating regimes. We quantify the fit (using the optimal points from the turbulence fitting indicated with the stars in **Fig 2A–2C**) in **Fig 2H**, which shows the statistical comparisons of the three regimes with functional connectivity (see **Methods**).

The results show that the best working point for the turbulence fitting for the noise regime is only giving a functional connectivity fitting mean  $\text{ErrFC} = 0.2594$ , which is significantly worse than both fluctuating and oscillatory regimes (Wilcoxon  $p < 0.001$ , comparing noise with fluctuations [mean  $\text{ErrFC} = 0.1422$ ]; Wilcoxon  $p < 0.001$ , comparing noise with oscillations [mean  $\text{ErrFC} = 0.2063$ ] in **Fig 2H**). On the other hand, the fluctuating and oscillatory regimes better fit the functional connectivity than the noise regime. However, in this case, the fluctuating regime is significantly better than the oscillatory regime (Wilcoxon  $p < 0.001$ , comparing fluctuations with oscillations box in **Fig 2H**).

We also evaluated the functional connectivity fitting for the same model-surrogates generated previously (see **Methods**) to compare with the corresponding optimal working point. The results clearly show significant differences with the obtained level of fitting with the optimal



working point of the models (Wilcoxon  $p < 0.001$ , comparing box fluctuations with *surr\_fluct* and box oscillations with *surr\_osc*).

Finally, in Fig 2I, we demonstrate the amplitude turbulence (the local Kuramoto parameter,  $R$ , see Methods) at the optimal fitting point of the three whole-brain model regimes contrasted with the empirical data (right subpanel) by rendering continuous snapshots for segments separated in time rendered on a flatmap of a brain hemisphere.

## Modelling results for less fine parcellation with 68 regions

Following the precise results of fitting the whole-brain model to the empirical data using a fine parcellation, we turned our attention to showing the fitting a less fine parcellation. We found that this was also not able to distinguish between fluctuating subcritical and oscillatory supercritical regimes. Specifically, we found that the level of fitting the empirical metastability defined as the standard deviation of the global Kuramoto order parameters is the same for both regimes.

We used during this second analysis a smaller brain parcellation, the Desikan-Killiany with 68 cortical regions of interest (ROIs), to be able to establish a node-level perturbative *in silico* protocol. We repeated the fitting procedure by exploring the parameter space  $(G, \beta)$  for the model in fluctuation supercritical and oscillatory subcritical regime but we also included the model considering the same absolute values of  $a$  than in fluctuation regime but with the opposite signs, that we called supercritical fluctuations. This parcellation is not suitable for computing amplitude turbulence, as is defined in Kawamura et al. [12] and Deco et al. [8], due to the lack of spatial resolution. We thus fitted the metastability, which is the most similar measure computable in coarser parcellation [16]. We found the pair  $(G, \beta)$  that minimizes the absolute difference between the empirical and simulated levels of metastability.

Fig 3 shows the results of fitting the Hopf whole-brain model in the two different regimes (fluctuations and oscillations) but also for the supercritical fluctuations,  $a \sim 0$  and  $a > 0$  (see upper row panel A, B and C). We computed for the Desikan-Killiany parcellation (upper row panel G) the fitting in terms of functional connectivity and metastability. For each of these regimes, we defined a grid of the parameter space  $(G, \beta)$ , and for each pair in the grid, we simulated 100 times the whole-brain dynamics, and we computed the level of fitting between the metastability (second row) and simulated and empirical FC (third row).

We found the optimal fitting for the level of metastability for each of the three scenarios, indicated with a star in the second row of Fig 3A–3C. Fig 3A shows the best fit for the fluctuating regime ( $a = -0.02$ ) with optimal  $(G, \beta) = (2.2, 0)$  with minimal absolute difference between the simulated and empirical metastability  $M$  (here  $eM = 4 \times 10^{-3}$ ). Fig 3B shows the best fit for the supercritical regime close to the bifurcation, supercritical fluctuations ( $a = 0.02$ ) with optimal  $(G, \beta) = (0.2, 1.4)$ , which fit the empirical data with  $eM = 7 \times 10^{-3}$ . Fig 3C shows the best fit for the oscillatory regime ( $a = 1.3$ ) with optimal  $(G, \beta) = (0.4, 2.2)$ , which also produces a good fit with  $eM = 1 \times 10^{-3}$ . We also computed the grid fitting for the FC, defined as the Euclidean distance between the simulated and empirical FC, for the tree scenarios (Fig 3D–3F), with a star in the grid indicating the optimal fit of metastability (which is the criterium for selecting the optimal working point since this is the most similar measure to turbulence). Note that these points do not correspond to the optimal fitting with FC. We found that the supercritical fluctuation regime behaves similar to the oscillatory regime showing an optimal working point with small coupling strength ( $G$ ) and  $\beta$  greater than one but the oscillatory regime provides better fit (Fig 3B). We replicated this analysis by expanding the region in the  $(G, \beta)$  parameter space to the same grid for both regimes. In S2 Fig, we display the level of fitting of turbulence and FC for a grid of  $G = [0-3.4]$  and  $\beta = [0-2.4]$  in 0.2 steps in both dimensions equally for the

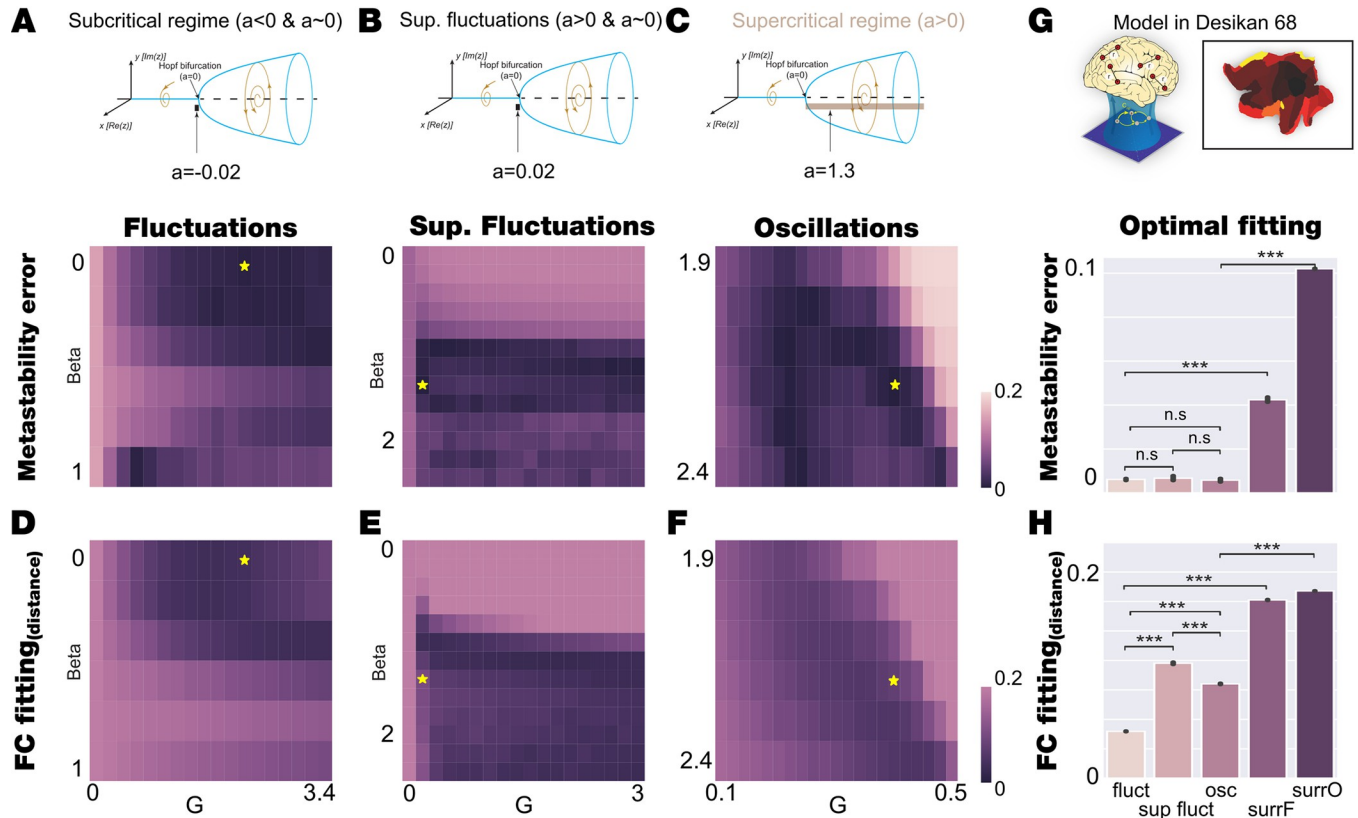


**Fig 3. Model Desikan-Killiary fitting of fluctuations and oscillatory for 1) Metastability and 2) FC fitting in.** A-C) We explored the bi-dimensional parameter space defined by  $\beta$  and  $G$  for fluctuating, supercritical fluctuations and oscillatory regime (bifurcation parameter  $a = -0.02$ ,  $a = 0.02$  and  $a = 1.3$ , respectively, indicated in the upper row) and computed the level of metastability error as the absolute difference between the empirical and simulated metastability. Yellow stars indicate the  $(\beta, G)$  combination that reaches the lowest metastability error in each regime. D-F) We explored the bi-dimensional parameter space defined by  $\beta$  and  $G$  for fluctuating, supercritical fluctuations and oscillatory regime computed the FC fitting as Euclidean distance between the empirical and simulated FC. Yellow stars indicate the  $(\beta, G)$  combination that reaches the lowest metastability error in each regime (the optimal working point obtained in panels A-C). G) The upper subpanel shows the model fitting scheme procedure in coarser Desikan-Killiary parcellation (the render on flatmap of the hemisphere stands for a scheme of brain regions considered in this parcellation). The bottom subpanel displays the barplot that indicates the statistical distribution of the metastability error obtained by simulating 20 trials with 100 subjects for each model regime with the parameters set at the corresponding working point. We also display the results of two model-based surrogates created by increasing the shear parameter of each model regime. The comparison between fluctuations, supercritical fluctuations and oscillations model's regimes at fitting the metastability shows that the two regimes are equally good (Wilcoxon, fluctuations vs oscillations  $P = 0.21$ ; fluctuations vs supercritical fluctuations  $P = 0.26$ ; and supercritical fluctuations vs oscillations  $P = 0.46$ ), while the rest of the comparisons are statistically significant (Wilcoxon,  $P < 0.001$ ). H) The barplot indicates the statistical distribution of the FC fitting obtained by simulating 20 trials with 100 subjects for each model regime at the corresponding working point defined as the minimum metastability error. We also display the results of two model-based surrogates created by increasing the shear parameter of each model. All comparisons are statistically significant (Wilcoxon,  $P < 0.001$ ).

<https://doi.org/10.1371/journal.pcbi.1010662.g003>

three regimes (we included the noise regime). We found that fluctuations and oscillatory regimes present the optimal working point in the regions we have previously analysed (red squares in S2 Fig).

The statistical comparison between the optimal working point of subcritical and supercritical model regimes (defined by the optimal fitting of the level of metastability, indicated with the stars in Fig 3A and 3C) is quantified in Fig 3G and 3H. We simulated 20 times the 100 repetitions of the whole-brain model at each regime working point and compared the level of metastability fitting and functional connectivity fitting (see Methods).

The results show that the fluctuating, supercritical fluctuating and oscillatory regimes are good at fitting the metastability and not significantly different (Wilcoxon, fluctuations vs oscillations  $P = 0.21$ ; fluctuations vs supercritical fluctuations  $P = 0.26$ ; and supercritical

fluctuations vs oscillations  $P = 0.46$ , first bars of Fig 3G). On the other hand, the fluctuating regimes better fit the functional connectivity than the supercritical fluctuations and oscillatory regime (Wilcoxon  $p < 0.001$ , for all comparisons in Fig 3H). Note that the supercritical fluctuations regime is similar to the supercritical regime in terms of parameter space working point and metastability fitting, but it produces a worst fitting in terms of functional connectivity, thus in the following we consider only the oscillatory regime for the study.

We also generated model-surrogates to compare with the corresponding optimal working point by setting the parameters of the model in the optimal working point but increasing  $\beta$ . Hence, we produced two surrogate models: *surr\_fluct* for the fluctuating model surrogates using  $a = -0.02$  and  $(G, \beta) = (2.2, 3)$  and *surr\_osc* for the oscillatory model surrogates using  $a = 1.3$  and  $(G, \beta) = (0.4, 3)$ . The results clearly show significant differences comparing with the level of metastability fitting obtained by the optimal working point of the model in different regimes (Wilcoxon  $p < 0.001$ , comparing fluctuation with *surr\_fluct* box and oscillations with *surr\_osc* boxes in the second row of Fig 3C). The same results were obtained for the fitting of the functional connectivity (Wilcoxon  $p < 0.001$ , comparing fluctuation with *surr\_fluct* box and oscillations with *surr\_osc* boxes of Fig 3F).

To complete the analysis, we computed within an equally and extended grid for the three regimes (noise, fluctuations and oscillations) other two metrics comparing the simulated and empirical FC, the traditional Pearson correlation and the structural similarity index (SSIM) [49]. This metric balances sensitivity to absolute (e.g. Euclidean distance) and relative (e.g. correlation distance) differences between the FC matrices because it is based on three different observables: the luminance, the contrast and the structure. We found that despite the correlation is not an optimal metric to constrain the models it shows that the fluctuation regime is performing better than the others (S3 Fig). In the same direction, the SSIM confirms that the fluctuation regime is the best model to fit FC and also is a good metric to define an optimal working point in the parameter space defined by  $[\beta, G]$ . For reference we display the yellow star representing the minimum found in metastability error exploration in Fig 3A and 3C.

The results also show that it could not distinguish between fluctuating subcritical and oscillatory supercritical regimes in coarser parcellation in terms of fitting the empirical data. We then focused our analysis on the perturbation response as an approach to disentangle between both models.

## Global strength-dependent perturbation distinguishes between fluctuating and oscillatory regimes

We implemented a global strength-dependent sustained perturbation that allows us distinguishing between fluctuating and oscillatory regimes for both the fine and coarse parcellations (Fig 4). We generated an *in silico* stimulus by adding an external periodic force applied equally to all nodes at the optimal working point in both model regimes (see Methods). We varied the strength of the external forcing  $F_0$  from 0 to 0.001 in steps of 0.0001, and for each amplitude, we simulated 100 times the perturbed and unperturbed model signals. We obtained the local and global Kuramoto order parameters (lKoP and gKoP) for the perturbed and unperturbed cases for the fine and coarse parcellation, respectively. We then computed the local and global Susceptibility and absolute Information Capacity as the mean and standard deviation of the subtraction between the perturbed and unperturbed lKoP and gKoP across trials (see Methods). We repeated this computation 20 times and Fig 4C–4F shows the mean and standard deviation across repetitions. The subcritical fluctuating regime shows a rapid increase of the level of local Susceptibility in the fine parcellation (Fig 4C) and the level of global Susceptibility in the coarse parcellation (Fig 4D). The global absolute Information Capability also rapidly

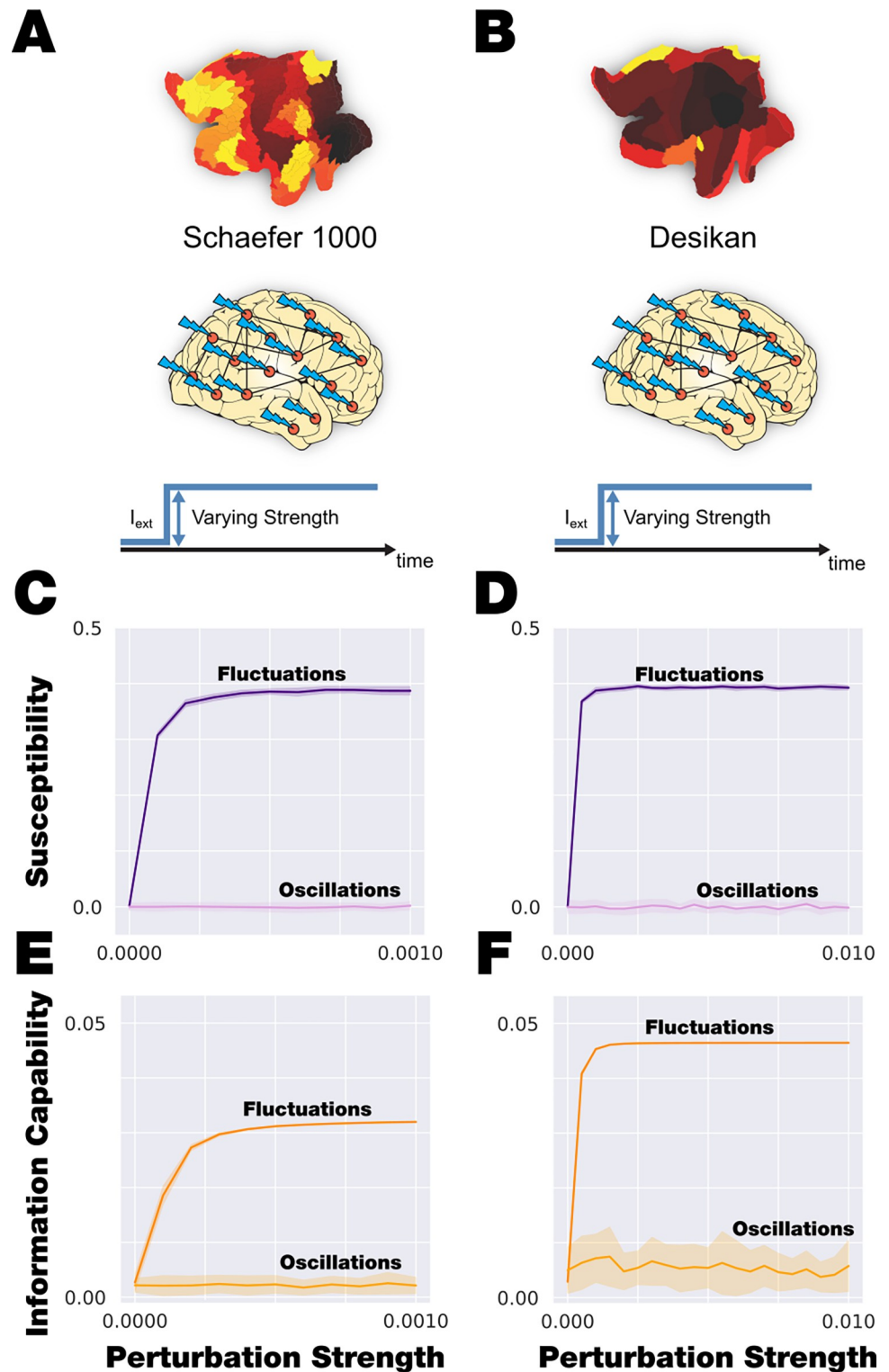


**Fig 4. Global and sustained strength-dependent perturbation.** A) We applied global strength-dependent, sustained perturbation in Schaefer1000 parcellation, and B) the same perturbation in Desikan-Killiany parcellation. C-D) The evolution of local and global Susceptibility (fine parcellation, panel C and coarse parcellation, panel D, respectively) as a function of perturbation strength. In dark purple is shown the response of the subcritical fluctuating regime, while in light purple, the behaviour of the supercritical oscillating regime. The subcritical regime is clearly more susceptible than the supercritical regime that is almost unaltered by the perturbation. E-F) The evolution of global absolute

Information Capacity (fine parcellation, panel E and coarse parcellation, panel F, respectively) as a function of perturbation strength. In dark orange is shown the response of the subcritical fluctuating regime, while in light orange, the behaviour of the supercritical oscillating regime. The subcritical regime clearly changes the Information Capacity with the perturbation strength comparing with the supercritical regime that is almost unaltered by the perturbation.

<https://doi.org/10.1371/journal.pcbi.1010662.g004>

increase while the forcing strength increases (Fig 4E and 4F dark colors). We have explored how the asymptotic values in both measures in the fluctuating regime depend on the bifurcation parameters ( $a$ ). To do so we slightly changed the value of  $a$  to keep in the subcritical regime but close to the bifurcation point. We found that the asymptote changes with the value of  $a$ : while  $a$  is closer to the bifurcation point ( $a = 0$ ) the system becomes less sensitive in terms of Susceptibility. The Information Capability behaves as opposite, while  $a$  is close to the bifurcation the system presents less Information Capability (S4 Fig). This could be interpreted that the fluctuation regime presents an optimal working point in terms of proximity of the bifurcation parameter to the bifurcation point ( $a = 0$ ) that balances the level of both measures.

In the supercritical oscillatory regime, the global Susceptibility and absolute Information Capability are constant in both parcellation along  $F_0$  (Fig 4C–4F light colours). It is remarkable that the level of these measurements in this regime keep almost zero for all the strength forcing range, showing that the model in that regime do not respond under this global perturbation.

### Local strength-dependent perturbation also distinguishes between fluctuating and oscillatory regimes

We then used local strength-dependent sustained and non-sustained perturbations that also allows us distinguishing between fluctuating and oscillatory regimes (Fig 5). This is demonstrated using the less fine parcellation. This reduction of the number of regions allowed us to define a node-by-node perturbative approach. Firstly, we explored the model's regime response by applying a sustained perturbation, and then we quantified the response to non-sustained external perturbation by the PCI.

### Susceptibility and information capability after local strength-dependent sustained perturbations

We systematically perturbed the model in each regime optimal working point by adding an external periodic force (see Fig 5A and Methods). We performed this *in silico* stimulation approach by forcing the 34 pairs of homotopic nodes (in the parcellation with 68 nodes) with forcing strength ranging from 0 to 0.02 in 0.001 steps. For each combination of nodes and amplitude, we ran 50 trials with 100 simulations, each computing the global Kuramoto Order parameter (gKoP) for the perturbed and unperturbed case (see Methods). We defined the node-level global Susceptibility and Information Capability as the mean and standard deviation across simulations of the subtraction between the node-perturbed and unperturbed gKoP, and we then averaged across trials. Fig 5A (second and third rows) shows the results for oscillatory (supercritical) and fluctuating (subcritical) regimes for both measurements. As in the global perturbation experiment, we noticed that the supercritical regime shows almost non-response under the perturbation, while the subcritical case presents variations across nodes and forcing amplitude. In this node-level perturbative approach, we can determine a hierarchy of perturbative effects by assessing node-by-node perturbation effect while the forcing amplitude increases. Fig 5A left panels shows a render onto brain cortex for both measurements in the subcritical regimen for 0.01 of forcing strength.

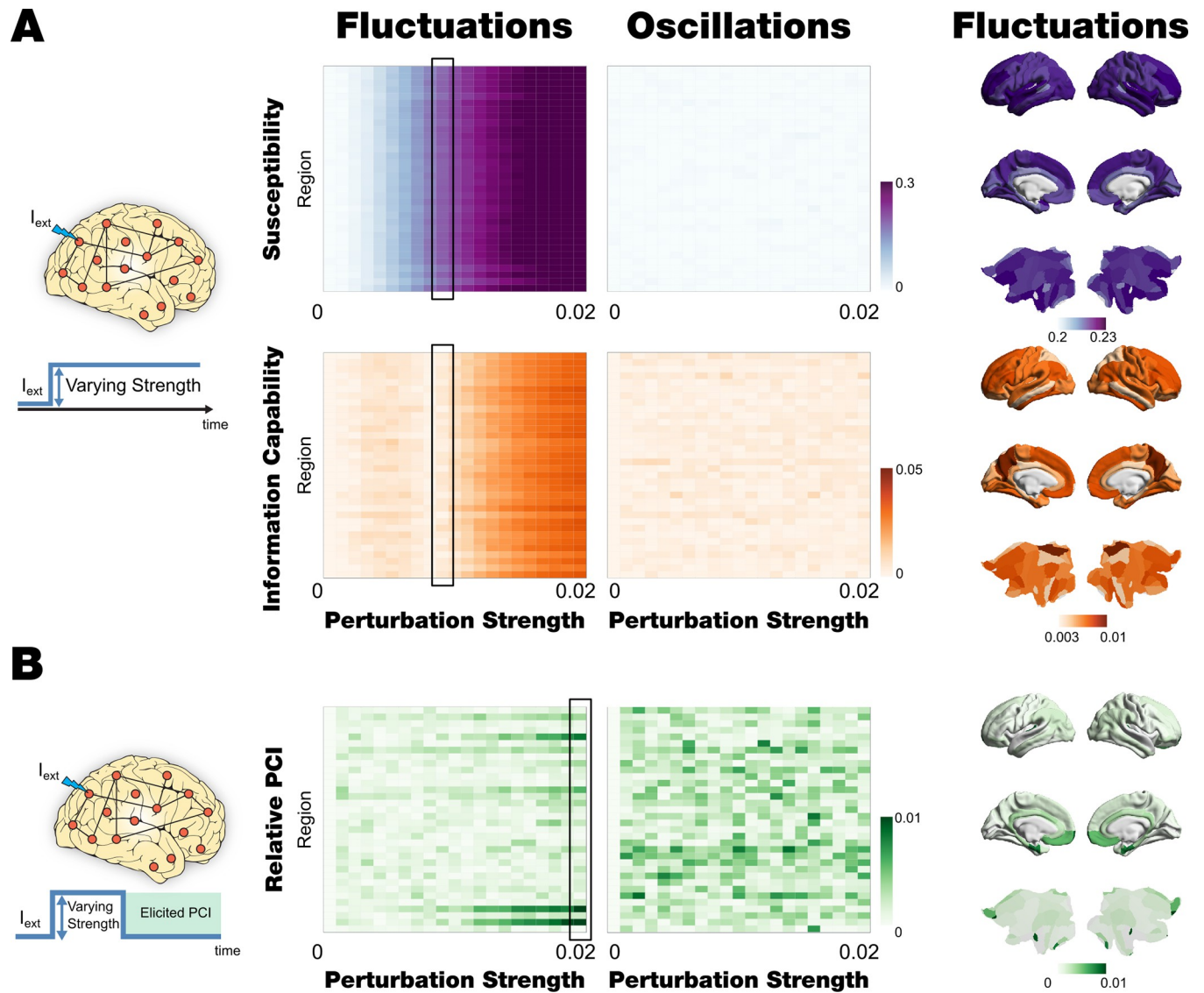


**Fig 5. Local and Sustained/non-sustained strength-dependent perturbation.** **A)** The evolution of Susceptibility (first row) and the absolute Information Capability (second row) as a function of the perturbation strength and the perturbed pairs of homotopic nodes. The middle left panel displays the results for the subcritical regime (fluctuations,  $a = -0.02$ ,  $G = 2.2$  and  $\beta = 0$ ), and the middle right panel shows the response of the supercritical regime (oscillations,  $a = 1.3$ ,  $G = 0.4$  and  $\beta = 2.2$ ). The right panels present the perturbative node hierarchy rendered onto the brain cortex for both measures (first and second row) for the case of a perturbation strength of 0.01 indicated with a box in middle left panel. **B)** Non-sustained PCI: The PCI is obtained by perturbing by pairs of homotopic nodes and different forcing amplitude. In the left column, the PCI results are obtained by perturbing the subcritical model in its corresponding working point with an external periodic force applied by pairs of homotopic nodes as a function of the amplitude of this forcing. In the right column, the same measurement is displayed but, in this case, for the supercritical model in its corresponding working point. The right panel shows the node-perturbative hierarchy in terms of PCI of each region for the maximum value of the forcing amplitude (indicated with black box in the middle-left panel) rendered onto a brain cortex.

<https://doi.org/10.1371/journal.pcbi.1010662.g005>

### PCI after local strength-dependent, non-sustained perturbations

We slightly modified our perturbative approach to bring the *in silico* stimulation protocol closer to *in vivo* experiments, as proposed by Massimini and colleagues [25]. We simulated the external perturbation as an additive external force by pairs of homotopic nodes as in previous sections, but in this case, we focused on the response after the perturbation ends. Specifically, we simulated 600 volumes with the perturbation active, and we then evaluated the evolution of

the signals in the following 200 volumes without perturbation. To investigate the behaviour of both model regimes, we adapted the PCI as is defined in Massimini et al. [25] to be applied on simulated BOLD signals (see [Methods](#)). This index gauges the amount of information contained in the integrated response to an external perturbation. [Fig 5B](#) displays the evolution of the PCI, computed as the normalised perturbed algorithmic complexity ( $\bar{c}$ ) minus the background algorithmic complexity ( $\bar{c}_{back}$ ), for both model regimes, for each pair of nodes and forcing strength. We found that in the oscillatory regime, the behaviour of the system after the perturbation is almost the same as the behaviour of the system without perturbation ( $\bar{c}_{back} \sim \bar{c}$ ), for all nodes and amplitudes ([Fig 5B](#) middle right panel). On the other hand, assessing the perturbation of the subcritical regime unveils a node hierarchy of the response under external perturbations ([Fig 5B](#) middle left panel).

These local responses under perturbations rendered onto the brain cortex for the maximal forcing amplitude is displayed in [Fig 5B](#) (right panel). It is remarkable that in the subcritical case, a set of nodes present the strongest response in terms of intensity (low values of PCI) and sensitivity (for lower forcing amplitudes). Most nodes present a moderate response for perturbations with forcing amplitude higher than 0.01, and other nodes remain unaltered.

### Regional heterogeneity and node-hierarchy perturbative organization

As shown in [Fig 6](#), we also investigated how the node-hierarchy established in the previous section can be related to other sources of regional heterogeneity. We used different external sources of local heterogeneity, the T1w:T2w ratio and the principal component of transcriptional activity of an extensive set of specific brain genes (see [Methods](#)). We also compared with the anatomical and functional connectivity strength of each region, computed as  $SC_{strength}(n) = \sum_{p=1}^N C_{np}$  and  $FC_{strength}(n) = \sum_{p=1}^N FC_{np}$  (well-known as Global brain connectivity, GBC), respectively, where C is the anatomical structural connectivity, and FC is the functional connectivity (see [Methods](#)). Finally, we compared the PCI node-hierarchy with the one found with global Susceptibility and Information Capability. We observed that the PCI hierarchical organisation is highly correlated with the other two perturbative measures obtained in the study. It is remarkable that this PCI node-hierarchy measure is computed after the perturbation ends, while the Susceptibility and Information Capability are computed during the perturbation.

### Revealing the causal mechanistic principles of empirical results modulating resting state networks using stimulation

Experimental research has shown that TMS stimulation of specific brain regions can differentially modulate specific networks [28,29]. We wanted to reveal the causal mechanistic principles and performed a network-level analysis testing the response of both model regimes (fluctuations and oscillations) using the Desikan-Killiany 68 parcellation, where each parcel belongs to one of the seven Yeo networks. The existing stimulation protocol was then applied in the same manner as in the previous analysis but now using a fixed forcing amplitude ( $F_0 = 0.01$ ). We computed the mean functional connectivity for the parcels belonging to each network using both fluctuating and oscillating regimes before and after the perturbation.

[Fig 7A](#) shows the seven Yeo resting state networks rendered on the medial and lateral surface of the right hemisphere of the brain. [Fig 7B](#) shows the differences between the perturbed and unperturbed FC for each model regime and the seven Yeo networks (RSN FC) as a function of the perturbed node. We found that the fluctuating regime enhances the functionality for all perturbed nodes and all networks, while the oscillatory regimen is essentially unaltered.

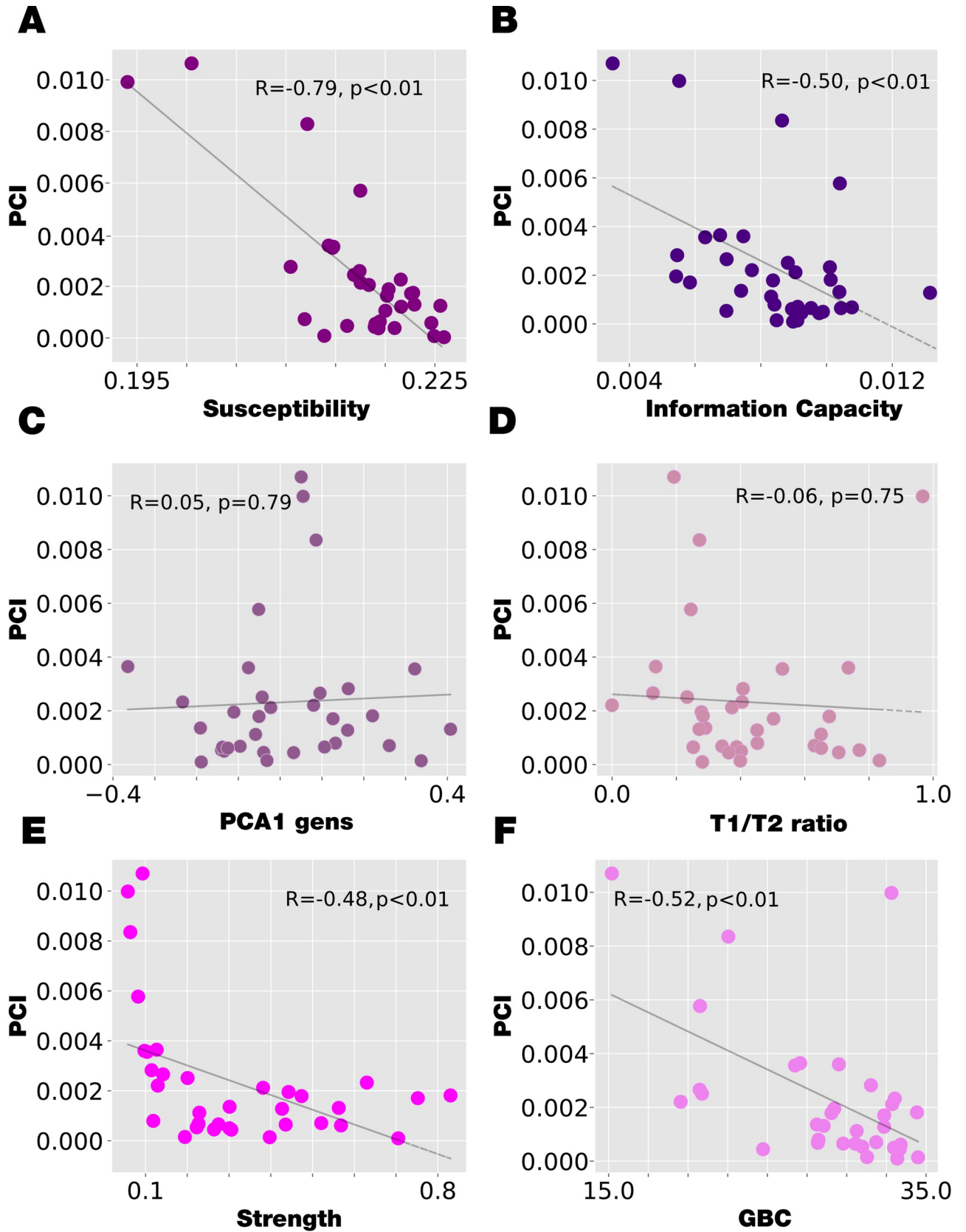




**Fig 6. The correlation between the node-level PCI and different sources of regional-level heterogeneity.** A-B) The correlation between node-level PCI and the node-level Susceptibility and Information Capacity are computed with significant negative correlation. C) The correlation between the node-level PCI and the first principal component of genes expression node information was computed. No correlation was found between variables. D) The same occurs in the correlation computed between the node-level PCI and the ratio between the T1/T2 MRI. E) The correlation between the node-level PCI and the node anatomical strength is computed obtaining a significant level of negative correlation. F) The correlation between the node-level PCI and the node functional connectivity strength (GBC) is computed obtaining a significant level of negative correlation.

<https://doi.org/10.1371/journal.pcbi.1010662.g006>

Fig 7C shows boxplots of the level of FC for each of the seven Yeo networks for the unperturbed and perturbed case for each model regime. We observed that not only the subcritical regime enhances the RSN FC for all network but also allows representing different levels depending on the network. In contrast, the subcritical regime is almost constant for all networks.

Given that we found that only the fluctuating regime is able to modulate the network after perturbation, we used this regime to stimulate a representative region (in red) of different resting state networks (Fig 7D, left column). This gives rise to a stabilisation of the respective network. Fig 7D (middle column) shows renderings of the normalised difference between the perturbed and unperturbed activity in term of RSN FC, thresholded to top the 15% for five resting state networks. The rightmost column showing the changes between the perturbed and unperturbed RSN FC as spiderplots of the elicited activity for each seven Yeo resting state network. As can be seen, the stimulated network is also the most stabilised. This result demonstrates the underlying principles for the empirical findings of modulation of resting state network following stimulation. This provides crucial empirical evidence for the fluctuating regime.

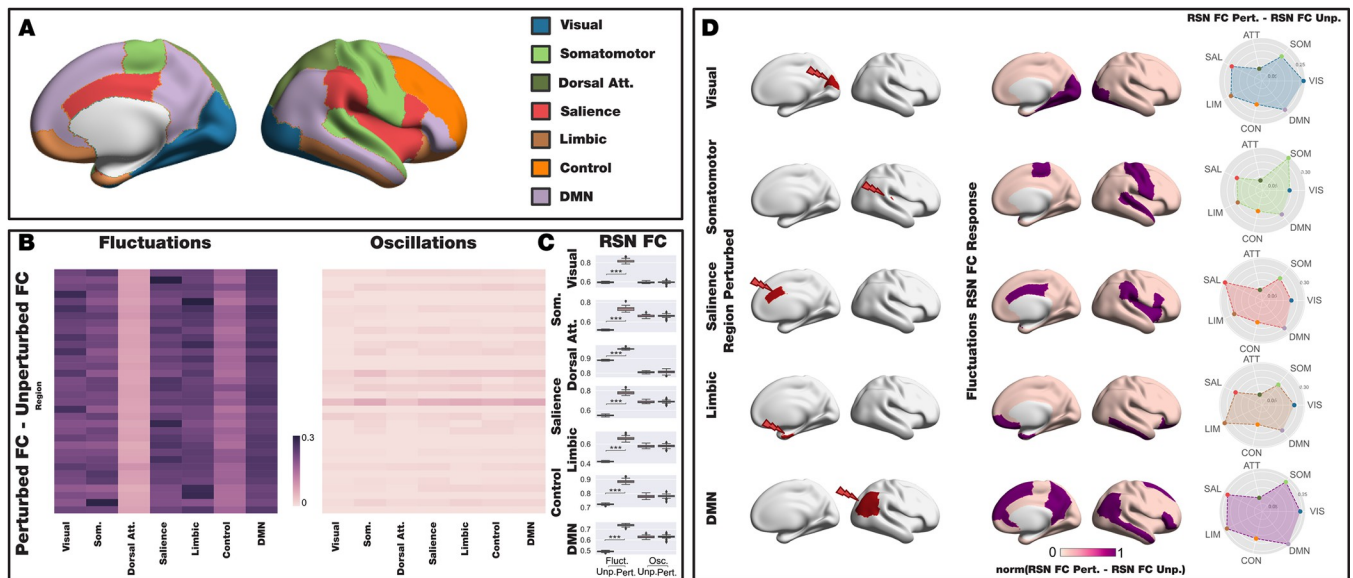


**Fig 7. Revealing the causal mechanistic principles of empirical results modulating resting state networks using stimulation.** A) For the reference, the seven Yeo resting state networks are rendered in the medial and lateral surface of the right hemisphere of the brain. B) Local and Sustained stimulation differentially enhances the resting state networks. The difference in the level of FC between the perturbed and unperturbed case is shown for the seven Yeo resting state networks as a function of the perturbed node. The subcritical regime enhances the FC for all networks and nodes, while the supercritical regime is much smaller and almost constant across nodes and networks. C) The seven subpanels show boxplots of the mean FC on each one of the seven Yeo resting state networks of the two model regimes in the unperturbed and perturbed case. The subcritical regime shows higher levels for the 7 networks and while the supercritical case remains almost unaltered with the perturbation. The significance of the results was assessed using the Wilcoxon rank-sum test, where \*\*\* represents  $p < 0.001$ . D) Left column shows a representative region (in red) in different resting state networks being perturbed in the fluctuating regime, which gives rise to a stabilisation of the respective network. The middle column is showing a rendering of the normalised difference between the perturbed and unperturbed activity in terms of RSN FC, thresholded to top 15%. The difference between the perturbed and unperturbed RSN FC can be seen in the spiderplots (right column), where the elicited activity is maximal for the stimulated network.

<https://doi.org/10.1371/journal.pcbi.1010662.g007>

## Discussion

Here we used whole-brain models to address a fundamental question in neuroscience of the origin of the fluctuations and oscillations found in global brain dynamics. We used a combined framework of a whole-brain model fitting to empirical data and strength-dependent perturbations to give a causal mechanistic description of human brain function. We found that the whole-brain model in the fluctuation regime more faithfully reproduces the functional connectivity when the regimes are tuned to capture the empirical level of turbulence. Furthermore, we investigated the computational capabilities of the different model regimes when are perturbed, and we demonstrated that the fluctuation regime presents the maximum responsiveness in terms of three perturbative measures: Susceptibility, Information capability and complex index. These results were obtained by assessing a large-scale Human Connectome neuroimaging dataset of 1003 participants, which were subsequently used for massive computational whole-brain modelling studies. Crucially, the underlying causal mechanistic principles of empirically reported modulation of the specific resting-state network can be explained by stimulation in the fluctuating regime. Overall, the present combined framework shows that the turbulence and functional connectivity fitting unveils that the model fluctuations regime is the best regime to capture empirical data properties and, in turn provides maximal flexibility for the human brain.

Specifically, we demonstrated that fluctuations and oscillations regimes of the Hopf whole-brain model are equally good at fitting the empirical data in terms of representing asynchronous and synchronous background dynamics, and in turns better than noise and supercritical fluctuations scenarios. Importantly, the functional connectivity is better represented by the fluctuation regime allowing us to disentangled which model regime are more suitable to represent empirical data. We also demonstrated that strength-dependent *in silico* perturbations, either local or global, sustained or non-sustained provide valuable insights to reveal the computational capacity on the model working point of each regime. The fluctuation regime shows more capacity to encode external stimuli than the others, consistent with the requirements of brain dynamics.

### **Fluctuating and oscillatory regimes computational capacities are distinguished by global strength-dependent perturbation**

We found that global strength-dependent and sustained perturbation distinguishes between the computational capacities of the fluctuating and oscillatory regimes. The Susceptibility and Information Capability level rapidly increases with amplitude strength in the subcritical fluctuating regime in fine-scale and coarser parcellations with 1000 and 68 regions, respectively. Conversely, the level of both measures in the supercritical oscillating regime remains almost constant along with the full range of amplitude strength. This result characterises both model regime in terms of responsiveness, where the subcritical model outperforms the supercritical model, providing a novel indication that the fluctuation regime is not only the regime that better fit empirical data but it also provides the highest response to external stimuli, as suggested by previous research [16,50,51].

Also, considering the similarities with the thermodynamic phase transition and bifurcations in dynamical system [52], this result can be interpreted in terms of the statistical criticality in brain dynamics. Previous research has demonstrated that the brain dynamics are poised near criticality, i.e., near the critical point of a phase transition [53,54], and at this point, the system has a higher susceptibility, where a small perturbation can be propagated along the whole system. Following this comparison, we can claim that the fluctuation regime dynamics are

comparable to staying close to the critical point of the phase transition. The result of both scenarios is to amplify the effect of perturbation and thus increase complexity.

### Local strength-dependent perturbation can distinguish between dynamical regimes

Furthermore, it is also possible to investigate the model's regime responses by applying local strength-dependent *in silico* perturbations. To this end, we used a less fine parcellation with 68 regions and systematically applied an external strength-dependent periodic force to all pairs of homotopic nodes. We also found that local strength-dependent and sustained perturbations efficiently discriminate between fluctuating and oscillatory regimes. We found that the node-by-node Susceptibility and Information Capacity increase with amplitude strength in the subcritical fluctuating regime, while in the supercritical regimen, both measures remain almost constant under the perturbations. Even more, in this node-level perturbative approach, we found a hierarchy of perturbative effect by assessing node-by-node response to the perturbation while the forcing amplitude increases in terms of Susceptibility and Information Capacity measures. These results extend the findings from previous research on elucidating the principles of deep brain stimulation [17], transcranial direct current stimulation [30] and recent research demonstrating in principle how to awaken a model of the sleeping brain [44,55] or how specific functional networks emerge after local stimulation [50,56].

### Local strength-dependent, non-sustained perturbations changes the PCI

Inspired by the pioneering results of perturbing the brain directly revealed by the empirical studies of Massimini and colleagues [25], we created a perturbative *in silico* strength-dependent local and non-sustained protocol which can provide testable empirical predictions in human participants by extending their use of PCI [7,25,26,57]. We found that in the oscillatory supercritical regime, the behaviour of the system after the perturbation is almost the same as without the perturbation for all nodes and amplitudes. The quantification of the response after the perturbation in the subcritical regime unveiled a node hierarchy of the response under external perturbations. As such, we were able to represent this hierarchy rendering onto the brain the value of the obtained PCI for each node at the maximal forcing amplitude.

### Hierarchical organisation revealed by perturbation of whole-brain model

We were able to reveal the hierarchical organisation through computing by PCI following local strength-dependent perturbations and comparing with other sources of regional heterogeneity. We used four of heterogeneity: 1) the myelination ratio (T1:T2w ratio), 2) the principal component of transcriptional activity of a large set of specific brain genes [31,58,59], 3) node-strength of structural and functional connectivity and 4) the hierarchies obtained for the Susceptibility and Information Capability computed for the local and sustained strength-dependent perturbations. We demonstrated that the PCI hierarchical organisation following local strength-dependent perturbations is highly correlated with the other two perturbative measures obtained in the study, which is correlated with the node-strength of structural and functional connectivity. Conversely, the PCI hierarchical organisation does not correlate with the T1:T2w ratio and PC1 of genes transcriptional activity.

These results show the power of perturbative *in silico* framework for addressing a fundamental question in neuroscience: namely, the role of the local fluctuations and oscillations in shaping the emergent global brain dynamical. By investigating the dynamics of the brain through a Hopf whole-brain model that allows switching from noisy asynchronous dynamics towards synchronous oscillations [16] we show that both dynamical regimes in microscopic

and macroscopic scales are associated with different global brain states: while the first seems to be the dynamical background need to support a responsive brain state, the second is related to reduced states of consciousness [6].

However, our framework is capable of distinguishing between both dynamical scenarios, but we also found that the perturbative hierarchy can provide an independent source of local information that can be used as *prior* in studies where heterogeneity plays a role [31,60]. These findings also pose a question regarding the relationship between each regional response capability to external stimuli and the role of fluctuations and oscillations. Future research could investigate heterogeneous models that allow each region to be in fluctuating or oscillatory regimes, the causal link between the local model regime and whole-brain susceptibility. Ultimately, this could help cast new light on the mechanistic interpretation of the local dynamics responsiveness in terms of the global response [1].

### Empirical evidence for the fluctuating regime

Finally, we evaluated the ability of stimulation in the fluctuating regime for modulating resting state networks by studying the functional connectivity over the entire network. This was inspired by experimental results demonstrating that different stimuli can bring about network-specific modulation [28,29,61]. The local and sustained stimulations in the whole-brain model may approximate invasive stimulation techniques such as deep brain stimulation, DBS [62], as well as non-invasive stimulation techniques such as transcranial magnetic stimulation, TMS [63]. We compared the dynamically responsive networks to external stimulus in different brain targets for both model regimes. In fluctuating/subcritical regime, the brain reacts to specific local stimulation with activity patterns that closely mimic the seven Yeo resting state networks [64]. We found that perturbing a region in a given resting state network led to stabilisation of that network. Our results are aligned with previous computational studies demonstrating that perturbative approaches are able to predict empirical observation, such as the emergence of large-scale functional networks [50,65]. Importantly, and supporting the superiority of the subcritical, fluctuating regime, in the supercritical oscillation regime the brain response remains almost unaltered when perturbing all nodes in the seven Yeo networks. In summary, preserving the resting state network structure is better represented by the subcritical regime, showing that dynamically responding brain networks are the outcome of a model working in fluctuation dynamical regime.

### Challenges and opportunities for *in silico* perturbation approaches

The findings have been made possible by the whole-brain modelling framework developed over the last decade [16,66–68]. A clear advantage of using such data-constrained whole-brain models is its potential use for studying stimulation protocols, as this enables an exhaustive search and optimization of all underlying parameters and locations *in silico*, and it may offer insights into the self-organization of widespread networks [18,55]. This strategy allowed to computationally assess the stimulation-induced transition between brain states as an insight of treatments prognosis [69], awakening from sleep stages [55], or defined perturbative metrics as a brain state characterization [44].

Nevertheless, despite there is much empirical evidence that clearly reflects the change of dynamics following perturbations [70–72], and the computational *in silico* results are really promising, the field awaits to confirm the whole-brain modelling predictive power. A potential path to doing such experiments could come from generative whole-brain models of the brain activity in animals (including non-human primates) [73–75] that allow performing both models and empirical tests [65]. In the future, these models could be used for investigating the

changes in brain state between awake and anaesthesia non-human primates [76], and suggest potential stimulation sites for transitioning between brain states, which can then be directly probed in these animal models. In this work, we pursued a novel approach by joining experimental and computational approaches. Our findings point to the possibility of strategically defined synthetic brain stimulations close to the specific experiments as an extension of the PCI [7,25].

Overall, here we have shed further light on a long-standing question in neuroscience, namely how and why brain states are characterised by complex, fluctuating and oscillating dynamics. Our results provide new evidence using strength-dependent perturbations of the whole-brain model fitting to the turbulence empirical level, revealing that brain function emerge and its responsiveness is better captured by fluctuating dynamics.

## Methods

### Neuroimaging ethics

The Washington University–University of Minnesota (WU-Minn HCP) Consortium obtained full informed consent from all participants, and research procedures and ethical guidelines were followed in accordance with Washington University institutional review board approval. Each participant reviewed and signed informed consent document. (Mapping the Human Connectome: Structure, Function and Heritability; IRB # 201204036).

### Neuroimaging participants

The data set was obtained from the Human Connectome Project (HCP) where we chose a sample of 1000 participants during resting state. The full informed consent from all participants was obtained by The Washington University–University of Minnesota (WU-Minn HCP) Consortium and research procedures and ethical guidelines were followed per Washington University institutional review board approval.

### Brain parcellations

To compute the empirical and simulated level of turbulence in brain dynamics defined as Deco et al. [8], we used the publicly available population atlas of cerebral cortical parcellation created by Schaefer and colleagues [43]. They provide several parcellations sizes available in surface spaces, as well as MNI152 volumetric space. We used the Schaefer parcellation with 1000 brain areas, estimated the Euclidean distances from the MNI space, and extracted the timeseries from the HCP surface space version.

Desikan and colleagues created an automated labelling system subdividing the human cerebral cortex into standard gyral-based neuroanatomical regions identifying 34 cortical ROIs in each hemisphere [77]. In the second section of this work, we used this parcellation to assess systematically the perturbation protocol ROI by ROI.

### Neuroimaging acquisition for fMRI HCP

The HCP web (<http://www.humanconnectome.org/>) provides the complete details for the acquisition protocol, participants information, and resting-state data. We used one resting-state acquisition of approximately 15 minutes, acquired for 1003 HCP participants scanned on a 3-T connectome-Skyra scanner (Siemens).

### Preprocessing and extraction of functional timeseries in fMRI resting data

The resting-state data were preprocessed using FSL (FMRIB Software Library), FreeSurfer, and the Connectome Workbench software [78] as reported in [10], which is described in detail

on the HCP website. Briefly, the preprocessing included correction for head motion, spatial and gradient distortions, intensity normalisation and bias field removal, registration to the T1-weighted image, transformation to the 2mm Montreal Neurological Institute (MNI) space, and FIX artefact removal [78,79]. Artefactual components were removed by using ICA+FIX processing (Independent Component Analysis followed by FMRIB's ICA-based X-noiseifier [80]). Preprocessed timeseries of all grayordinates are in HCP CIFTI grayordinates standard space, and available in the surface-based CIFTI file for each participant.

Custom-made Matlab scripts were applied using the `ft_read_cifti` function (Fieldtrip toolbox [81]) to extract the timeseries of the grayordinates in each node of the Schaefer parcellation. Furthermore, the BOLD timeseries were transformed to phase space by filtering the signals within the range 0.008–0.08 Hz [2], and the low-pass cut-off to filter the physiological noise, which tends to dominate higher frequencies [2,82].

### Structural connectivity using dMRI

The structural connectivity was obtained from the Human Connectome Project (HCP) database, which contains diffusion spectrum and T2 weighted imaging data from 32 participants. The acquisition parameters are described in detail on the HCP website. Briefly, the neuroimaging data were processed using a generalised q-sampling imaging algorithm developed in DSI studio (<http://dsi-studio.labsolver.org>). A white-matter mask was estimated by segmenting the T2-weighted images and images were co-registered to the b0 of the diffusion data by using SPM12. In each participant, 200,000 fibres were sampled within the white-matter mask. Fibres were transformed into MNI space using Lead-DBS [83]. We used the standardised methods in Lead-DBS to produce the structural connectomes for both Schaefer 1000 parcellation [43] and Desikan-Killiany 68 parcellation [77], where the connectivity was normalised to a maximum of 0.2. The preprocessing implemented is freely available in the Lead-DBS software package (<http://www.lead-dbs.org/>) and is described in detail by Horn and colleagues [84].

### Whole-brain model

Whole-brain models have been used during the last decade to describe the most important features of brain activity. These models provide an optimum balance between complexity and realism, based on the fact that despite the macroscopic collective brain behaviour is an emergent of millions of small units interacting endowed with independent properties. One of the macroscopic dynamical features is that the collective behaviour dynamics can range from fully synchronous to stable asynchronous state governed by random fluctuations. The simplest dynamical system capable of presenting both behaviours is the one described by a Stuart Landau non-linear oscillator, which is mathematically described by the normal form of a supercritical Hopf bifurcation:

$$\frac{dz}{dt} = (a + i\omega)z - (1 + i\beta)z|z|^2 \quad (1)$$

Where  $z$  is a complex-valued variable ( $z = x+iy$ ),  $\omega$  is the intrinsic frequency of the oscillator, and  $\beta$  is the shear factor. The bifurcation parameter  $a$  changes qualitatively the nature of the solutions of the system, if  $a > 0$  the system engage in a limit cycle and presents self-sustained oscillations so-called the supercritical regime and when  $a < 0$  the dynamics decay to a stable fixed point so-called the subcritical regime (Fig 1E).

The coordinated dynamics of the resting state activity are modelled by introducing coupling between these oscillators. Previous research has demonstrated that whole-brain models based on Stuart Landau oscillators ruling the local dynamical behaviour have the capability to

describe the time average behaviour (static functional connectivity) and dynamical behaviour (functional connectivity dynamics–FCD) on brain dynamics when the coupling between the oscillators is determined by the structural connectivity [16,19,23]. Here, based on recent work, we assume that the coupling is determined by a combination of the *exponential distance rule* (EDR) and the long-range connection present in the structural connectivity (EDR-LR) [10]. The mathematical expression that rules this coupling factor is:

$$C_{ij} = e^{-\lambda * r_{ij}} + LR \tag{2}$$

Where,  $\lambda$  stands for the exponential space decay fitted from empirical data and fixed at  $\lambda = 0.18 \text{ mm}^{-1}$  [8],  $r_{ij}$  is the Euclidian distance between the node  $i$  and  $j$  and LR are the long-range connections extracted from the anatomical structural connectivity. The dynamical of the region (node)  $i$  in the coupled whole-brain system is described in cartesian coordinates:

$$\frac{dRe(z_i)}{dt} = \frac{dx_i}{dt} = a_i x_i + [x_i^2 + y_i^2] (\beta y_i - x_i) - \omega_i y_i + G \sum_{j=1}^N C_{ij} (x_j(t) - x_i) + v_i \eta_i(t) \tag{3}$$

$$\frac{dIm(z_i)}{dt} = \frac{dy_i}{dt} = a_i y_i - [x_i^2 + y_i^2] (\beta x_i + y_i) - \omega_i x_i + G \sum_{j=1}^N C_{ij} (y_j(t) - y_i) + v_i \eta_i(t)$$

Where  $x_j$  is the dynamical variable that simulates the BOLD signal of region  $j$  obtained from functional magnetic resonance (fMRI). An additive Gaussian noise with standard deviation  $v$  is represented by  $\eta_i(t)$  and  $G$  is a factor that scales the coupling strength equally for all the nodes. This whole-brain model has been shown to reproduce essential features of brain dynamics observed in different neuroimaging recordings [16,41] in the subcritical regime (i.e.,  $a < 0$ ) and no shearing effect ( $\beta = 0$ ).

### Model optimal working point in ( $\beta, G$ ) parameter space and regime comparison

We incorporate the shear factor as a global fitting parameter and the global scaling factor ( $G$ ). In the first part of this study, we fit the level of turbulence using the Schaefer 1000 parcellation. We perform an exhaustive exploration of the parameter space ( $\beta, G$ ), seeking the optimal working point of the model in noise regime ( $a = -1.3$ ), subcritical regime ( $a = -0.02$ ) and supercritical regime ( $a = 1.3$ ). In the supercritical case, we explore a grid of  $\beta = [1.7; 2.5]$  and  $G = [0.13; 0.22]$  in 0.1 steps, whereas in the noise and subcritical case we explore a grid of  $\beta = [0; 0.8]$  and  $G = [0.45; 1.8]$  in steps of 0.1 and 0.15, respectively. We generate 100 simulations with the same number of volumes (1200 volumes) and sampling rate (0.72 s) of empirical data for each pair ( $\beta, G$ ) on the grid and compute the simulated level of turbulence and functional connectivity as the Pearson correlation between nodes signals. We estimated the fitting of level of turbulence as the absolute value of the difference between the average of the empirical and simulated level of turbulence and the functional connectivity fitting as the Euclidean distance between the empirical and simulated FC.

For comparing how good each regime is at fitting the empirical data, we generate 100 simulations with the same number of volumes (1200 volumes) and sampling rate (0.72 s) as the empirical data at the optimal working point of the three regimes. We compute the error of turbulence fitting and the FC fitting as the average value across simulations. We repeat 20 times each set of simulations. We also reproduce the same amount of simulation for two model surrogates consisting in increase to 6 the value of the shear parameter ( $\beta$ ) for the optimal working point of the subcritical and supercritical regime.

In the second part of this study, we change the parcellation to the Desikan-Killiany parcellation with 68 nodes. The advantage of this parcellation is that it allows us to establish a

systematical perturbation protocol at node scale within affordable computational time. The disadvantage is that the level of turbulence definition, as in Deco et al. [8], is not computable in small parcellations, i.e., low distance resolution. We fit the level of metastability by computing the absolute difference between the empirical and simulated brain signals. We perform an exhaustive exploration of the parameter space ( $\beta, G$ ), seeking the optimal working point of the model only in supercritical regime ( $a = 1.3$ ) and subcritical regime ( $a = -0.02$ ), we discarded the noise regime in light of the results obtained in the fine parcellation analysis. In the supercritical case, we explore a grid of  $\beta = [1.9; 2.4]$  and  $G = [0.1; 0.5]$  in 0.1 and 0.02 steps respectively, while in the subcritical case we explore a grid of  $\beta = [0; 1]$  and  $G = [0; 3.4]$  in steps of 0.2 both. We generate 100 simulations with the same number of volumes (1200 volumes) and sampling rate (0.72 s) of empirical data for each pair ( $\beta, G$ ) on the grid and compute the simulated level of metastability and the functional connectivity fitting using the Euclidean distances between the empirical and simulated FC (see [Methods](#) below). For comparing how good each regime is at fitting the empirical data, we generate 100 simulations with the same number of volumes (1200 volumes) and sampling rate (0.72 s) as the empirical data at the optimal working point of the three regimes. We compute the error of metastability fitting and the FC fitting as the average value across simulations. We repeat 20 times each set of simulations. We also reproduce the same amount of simulation for two model surrogates, which increase to 3 the value of the shear parameter ( $\beta$ ) for the optimal working point of the subcritical and supercritical regimes.

### Perturbative in silico protocol

We model an external oscillatory perturbation and investigate the response of the whole-brain model fitted to the aforementioned observables in each parcellation in different model regimes. The stimulus was represented as an external additive periodic forcing term, given by  $F_j = F_{0j} \cos(\omega_j t) + iF_{0j} \sin(\omega_j t)$ , in the corresponding real and imaginary part of the node  $j$  equation ([Eq 3](#)). The purpose of this perturbation was to model the effects of external stimulation (TMS, tACS). In the first part of this study, we simulate a global strength-dependent, sustained perturbation by applying the external forcing equally for all nodes ( $F_0$ ) at the node's empirical frequency average ( $\omega$ ). We vary the forcing strength ( $F_0$ ) from 0 to 0.001 in 0.0001 steps. We then generate 50 trials with 50 simulations each one for each step and compute the perturbed and unperturbed local (global) Kuramoto order parameter in the fine (coarse) parcellation. Finally, we assess the behaviour of each model regime using the computation of local Susceptibility and Information capability in fine parcellation and through the global Susceptibility and local Information capability in coarser parcellation (see [Methods](#) below).

In the second part of the study, we simulate local strength-dependent, sustained and non-sustained perturbations adding an external periodic force by pairs of homotopic nodes. In this way, we obtain 34 *in silico* experiments varying the amplitude of the force,  $F_0$ , from 0 to 0.02 in steps of 0.005 and generating 50 trials with 100 simulations each one for each step.

We assess the model's response to the sustained perturbation by computing the global Susceptibility and Information Capacity by pairs of homotopic nodes and amplitude. We assess the model's response to the non-sustained perturbation through computing the perturbative complexity index (PCI) for each forcing amplitude and pair of perturbed nodes.

### Measure of amplitude turbulence

The level of amplitude turbulence measure comes from the seminal studies by Kuramoto investigating turbulence in coupled oscillators [11] and by Deco and Kringelbach that applied this concept to whole-brain dynamics [8]. Specifically, in a coupled oscillator framework, the



Kuramoto local order parameter (IKoP) represents a spatial average of the complex phase factor of weighted coupling of local oscillators. The modulus of the Kuramoto local order parameter ( $R_n(t)$ ) is considered a measure of the local level of synchronization and is computed as:

$$R_n(t)e^{i\theta(t)} = \sum_p \left[ \frac{C_{np}}{\sum_q C_{nq}} \right] e^{i\varphi_p(t)} \tag{4}$$

where  $\varphi_p$  is the phase of the BOLD signal of the node  $p$  and  $C_{np}$  is the strength of the coupling between node  $n$  and  $p$  determined by the exponential distance rule (first term of Eq 2). We then compute the amplitude turbulence,  $D$ , as the standard deviation across time and space of the modulus of the IKoP,  $R_n(t)$ :

$$D = \sqrt{\langle R^2 \rangle - \langle R \rangle^2} \tag{5}$$

where brackets stand for the average across time and space.

We computed the error in fitting the level of turbulence ( $eD$ ) as the absolute value of the difference between the empirical and simulated level of turbulence:

$$eD = \text{abs}(D_{sim} - D_{emp}) \tag{6}$$

### Measure of metastability

The level of metastability measure was implemented in previous research to characterize the dynamics of the fluctuations in brain activity in different brain states [16,19,41]. Briefly, the metastability denotes the variability of the global synchronization as measured by the Kuramoto order parameter ( $gR(t)$ ):

$$gR(t)e^{i\theta(t)} = \sum_p^n e^{i\varphi_p(t)} / n \tag{7}$$

where  $\varphi_p$  is the phase of the BOLD signal of the node  $p$  and  $n$  is the total number of nodes in the parcellation. Thus, the metastability is the standard deviation of  $gR(t)$  across time:

$$M = \sqrt{\langle gR^2 \rangle - \langle gR \rangle^2} \tag{8}$$

The fitting of metastability is defined as the absolute difference between the empirical and simulated level of metastability:

$$eM = \text{abs}(M_{sim} - M_{emp}) \tag{9}$$

### Measure of susceptibility

We define the whole-brain model susceptibility as the brain’s sensitivity to the processing of external periodic stimulations. We perturb the Hopf model in the supercritical and subcritical regime by adding an external periodic force with different amplitudes (see Methods, perturbative in silico protocols). We estimate the sensitivity of the perturbations on the spatiotemporal dynamics following previous work, which determines the susceptibility in a system of coupled oscillators based on the response of the Kuramoto order parameter [33]. In the first part of this study, we extend this concept by assessing the variability of the modulus of the local Kuramoto order parameter, i.e.,  $R_n^{F_0}(t)$  for the perturbed case for each value of forcing amplitude ( $F_0$ ), and  $R_n(t)$  for the unperturbed case. We define local susceptibility in the following way:

$$\chi_{local}(F_0) = \langle \langle \langle R_n^{F_0}(t) \rangle_t - \langle R_n(t) \rangle_t \rangle_{trial} \rangle_s \tag{10}$$

where  $\langle \rangle_t$ ,  $\langle \rangle_{trials}$  and  $\langle \rangle_s$  are the mean averages across time, trials, and space, respectively.

In the second part of the study, we estimate the sensitivity of these perturbations by measuring the modulus of the global Kuramoto order parameter (gKoP),  $gR(t)$ , as a measurement of the global level of synchronization of the  $n$  nodes signal [16]:

We compute the gKoP ( $gR_m^{F_0}(t)$ ) for the perturbed case for each value of forcing amplitude ( $F_0$ ) and pairs of perturbed nodes ( $m$ ) and  $gR(t)$  for the unperturbed case. We define the global Kuramoto order parameter and global Susceptibility as follows:

$$\chi_{global}(F_0, m) = \langle \langle gR_m^{F_0}(t) \rangle_t - \langle gR(t) \rangle_t \rangle_{trial} \quad (11)$$

where  $\langle \rangle_t$   $\langle \rangle_{trials}$  are the mean averages across time and trials.

### Measure of information capability

We define the Information Capability as a measure to capture how different external stimulations are encoded in the dynamics. We perturb the model in both regimes as above and compute for the first part of the study the perturbed and non-perturbed local Kuramoto order parameter for each forcing amplitude and, for the second part, the global Kuramoto order parameter for each forcing amplitude and perturbed nodes. The analytical computation of the Information Capability is through the standard deviation across trials of the difference between the perturbed Kuramoto order parameters and unperturbed ones. For the first part of the study, when we compute the local Kuramoto order parameter is computed as follows:

$$IC_{loc}(F_0) = \langle \langle (\langle R_n^{F_0}(t) \rangle_t - \langle R_n(t) \rangle_t)^2 \rangle_{trial} - (\langle \langle R_n^{F_0}(t) \rangle_t - \langle R_n(t) \rangle_t \rangle_{trial})^2 \rangle_s \quad (12)$$

For the second part of the work, we compute the global Kuramoto order parameter and perturb by pairs of homotopic nodes ( $m$ ) at different forcing amplitude ( $F_0$ ):

$$IC_{gl}(F_0, m) = \langle \langle (gR_m^{F_0}(t) - gR(t))^2 \rangle_{trial} - (\langle \langle gR_m^{F_0}(t) - gR(t) \rangle_{trial} \rangle)^2 \quad (13)$$

We then define absolute Information Capability (IC) as the absolute difference between the IC at each forcing strength and the IC at zero-forcing for the global and local.

### Measure of PCI

We compute the perturbation complexity index (PCI) following the study of Casali and colleagues [25], where they implemented this index to characterise the empirical response to external stimuli in different states of consciousness. We simulate the perturbation described above by an external periodic force applied by pairs of homotopic nodes with different forcing amplitudes. For each case, we generate 100 simulations with 800 volumes and a sampling rate (0.72 s) for the optimal working point of each model regime. The first 600 volumes with the external force perturbing the system and the last 200 volumes without the perturbation:

$$\bar{c}_L = c_L \frac{\log_2 L}{LH(L)} \quad (14)$$

where  $c_L$  is the Lempev-Ziv complexity as a measure of algorithmic complexity [85],  $L$  is the length of the binary sequence, and  $H(L)$  is the source entropy of a sequence of length  $L$  that normalise the measure in order to be 1 to random sequences. For this purpose, we create a binary spatiotemporal distribution by z-scored the simulated times series after perturbation,  $ts(n,t)$ , where if  $ts_{zscore}(n,t) > 2 = 1$  and if  $ts_{zscore}(n,t) < -2 = 0$ . We then average across simulations the computed PCI for each pair of nodes and each forcing amplitude. To assess the response under external perturbation of both regimens, we compared the computed value after perturbation,  $\bar{c}_L(F_0, m)$ , with the background level computed over simulated signal in each regime

working point without perturbation ( $\bar{c}_L^{back}$ )

$$PCI(F_0, m) = \bar{c}_L(F_0, m) - \bar{c}_L^{back} \quad (15)$$

## Regional heterogeneity data

Here, we use different sources of regional heterogeneity to compare with the node-level hierarchy established by the perturbation response. We consider the ratio T1w:T2w, which is sensitive to myelin content [86] and the first principal component (PC1) of transcriptional activity for 1,926 brain-specific genes. To this end, we use data from the Allen Institute Human Brain Atlas (AHBA), which comprises microarray data quantifying the transcriptional activity of >20,000 genes in >4,000 different tissue samples distributed throughout the brain, taken from six post-mortem samples. The AHBA data were processed following the pipeline developed in Arnatkeviciute et al. [59]. To adapt the gene expression information into node-level heterogeneity information to Desikan-Killiany parcellation, we used the same approach explained in previous work [31].

## Statistical analyses

Differences in model fits to empirical properties, as well as the resting state network enhancement, were assessed using pairwise Wilcoxon rank sum tests. The significance of each model regime fitting was assessed by comparing with model surrogates.

## Supporting information

**S1 Fig. Model Schaefer1000 fitting of noise, fluctuations, and oscillatory for turbulence and FC using the Structural Connectivity (SC).** A-C) We explored the bi-dimensional parameter space defined by  $\beta$  and  $G$  for noise, fluctuating and oscillatory regime as we performed in Fig 2 (bifurcation parameter  $a = -1.3$ ,  $a = -0.02$  and  $a = 1.3$ , respectively, indicated in upper row). We computed the level of amplitude turbulence error as the absolute difference between the empirical and simulated turbulence. Yellow stars indicate the  $(\beta, G)$  combination that reaches the lowest turbulence error in each regime. E-G) We explored the bi-dimensional parameter space defined by  $\beta$  and  $G$  for noise, fluctuating and oscillatory regime computed the FC fitting as Euclidean distance between the empirical and simulated FC. Yellow stars indicate the  $(\beta, G)$  combination that reaches the lower turbulence error in each regime (the optimal working point obtained in panels A-C). (TIF)

**S2 Fig. Model Desikan-Killiany fitting of noise, fluctuations and oscillatory for Metastability and FC fitting.** We explored an extended the bi-dimensional parameter space defined by  $\beta$  and  $G$  equally for noise, fluctuating and oscillatory regime (bifurcation parameter  $a = -1.3$ ,  $a = -0.02$  and  $a = 1.3$ , respectively, indicated in the upper row) and computed the level of metastability error as the absolute difference between the empirical and simulated metastability. Yellow stars indicate the  $(\beta, G)$  combination that reaches the lowest metastability error in each regime (second row). We explored the bi-dimensional parameter space defined by  $\beta$  and  $G$  for noise, fluctuating and oscillatory regime computed the FC fitting as Euclidean distance between the empirical and simulated FC (third row). Yellow stars indicate the  $(\beta, G)$  combination that reaches the lowest metastability error in each regime (the optimal working point obtained in panels second row). We explored the same grid for the three regimes for comparison indicating with red squares the region that were computed in Fig 3. (noise regime were

not computed in Fig 3 but we did include in this figure). We confirm that the regions explored in Fig 3 are the optimal working point zones in fluctuating and oscillation regimes.

(TIF)

**S3 Fig. Model Desikan-Killiany fitting of noise, fluctuations and oscillatory for Pearson correlation and structural similarity index (SSIM) between simulated and empirical FC.**

We explored the extended bi-dimensional parameter space defined by  $\beta$  and  $G$  for noise, fluctuating and oscillatory regime (bifurcation parameter  $a = -1.3$ ,  $a = -0.02$  and  $a = 1.3$ , respectively, indicated in the upper row) and computed the Pearson correlation (second row) and SSIM (third row) between the empirical and simulated FC. Yellow stars indicate the  $(\beta, G)$  combination that reaches the lowest metastability error in each regime from S2 Fig.

(TIF)

**S4 Fig. Global Susceptibility and Information Capability in the fluctuating regime dependence on the bifurcation parameter.**

We estimated the Susceptibility and Information Capability of the model at its optimal working point when it is perturbed as a function of the perturbation strength in Desikan-Killiany parcellation. We found that when the value of  $a$  is closer from the bifurcation point ( $a = 0$ ), the Susceptibility increases (left panel) and the Information Capability decreases (right panel). Red lines stand for the asymptotic values reached for  $a = -0.02$  displayed in Fig 4.

(TIF)

## Author Contributions

**Conceptualization:** Yonatan Sanz Perl, Enzo Tagliazucchi, Morten L. Kringelbach, Gustavo Deco.

**Data curation:** Morten L. Kringelbach.

**Formal analysis:** Yonatan Sanz Perl, Gustavo Deco.

**Investigation:** Yonatan Sanz Perl, Anira Escrichs, Morten L. Kringelbach, Gustavo Deco.

**Methodology:** Yonatan Sanz Perl, Anira Escrichs, Enzo Tagliazucchi, Morten L. Kringelbach, Gustavo Deco.

**Software:** Yonatan Sanz Perl, Morten L. Kringelbach, Gustavo Deco.

**Supervision:** Morten L. Kringelbach, Gustavo Deco.

**Writing – original draft:** Yonatan Sanz Perl, Morten L. Kringelbach, Gustavo Deco.

**Writing – review & editing:** Yonatan Sanz Perl, Anira Escrichs, Enzo Tagliazucchi, Morten L. Kringelbach, Gustavo Deco.

## References

1. Destexhe A, Contreras D. Neuronal Computations with Stochastic Network States. *Science* (80-). 2006; 314: 85–90. <https://doi.org/10.1126/science.1127241> PMID: 17023650
2. Fox M. The human brain is intrinsically organized into dynamics, anticorrelated functional networks. *Proc Natl Acad Sci USA*. 2005; 102: 9673–9678. <https://doi.org/10.1073/pnas.0504136102> PMID: 15976020
3. Biswal B, Yetkin F, Haughton V, Hyde J. Functional connectivity in the motor cortex of resting human brain using echo-planar MRI. *Magn Reson Med Off J Soc Magn Reson Med / Soc Magn Reson Med*. 1995; 34: 537–541. <https://doi.org/10.1002/mrm.1910340409> PMID: 8524021
4. Raichle M, Mintun M. Brain work and brain imaging. *Annu Rev Neurosci*. 2006; 29: 449–476. <https://doi.org/10.1146/annurev.neuro.29.051605.112819> PMID: 16776593

5. Mantini D, Perrucci M, Del Gratta C, Romani G, Corbetta M. Electrophysiological signatures of resting state networks in the human brain. *Proc Natl Acad Sci USA*. 2007; 104: 13170–13175. <https://doi.org/10.1073/pnas.0700668104> PMID: 17670949
6. Goldman JS, Tort-Colet N, di Volo M, Susin E, Bouté J, Dali M, et al. Bridging Single Neuron Dynamics to Global Brain States. *Front Syst Neurosci*. 2019; 0: 75. <https://doi.org/10.3389/fnsys.2019.00075> PMID: 31866837
7. Goldman JS, Kusch L, Yalcinkaya BH, Depannemaecker D, Nghiem T-AE, Jirsa V, et al. Brain-scale emergence of slow-wave synchrony and highly responsive asynchronous states based on biologically realistic population models simulated in The Virtual Brain. *bioRxiv*. 2020; 2020.12.28.424574. <https://doi.org/10.1101/2020.12.28.424574>
8. Deco G, Kringelbach ML. Turbulent-like Dynamics in the Human Brain. *Cell Rep*. 2020; 33: 108471. <https://doi.org/10.1016/j.celrep.2020.108471> PMID: 33296654
9. Deco G, Kemp M, Kringelbach ML. Leonardo da Vinci and the search for order in neuroscience. *Curr Biol*. 2021; 31: R704–R709. <https://doi.org/10.1016/j.cub.2021.03.098> PMID: 34102114
10. Deco G, Perl YS, Vuust P, Tagliazucchi E, Kennedy H, Kringelbach ML. Rare long-range cortical connections enhance human information processing. *Curr Biol*. 2021 [cited 18 Sep 2021]. <https://doi.org/10.1016/j.cub.2021.07.064> PMID: 34437842
11. Kuramoto Y. *Chemical Oscillations, Waves, and Turbulence*. Springer-Verlag. 1984. Available: [https://books.google.es/books?hl=en&lr=&id=4ADt7smO5Q8C&oi=fnd&pg=PA1&ots=H17BQU2iwr&sig=KGBj5OICty2zvhoAChDp2bEG3bw&redir\\_esc=y#v=onepage&q&f=false](https://books.google.es/books?hl=en&lr=&id=4ADt7smO5Q8C&oi=fnd&pg=PA1&ots=H17BQU2iwr&sig=KGBj5OICty2zvhoAChDp2bEG3bw&redir_esc=y#v=onepage&q&f=false)
12. Kawamura Y, Nakao H, Kuramoto Y. Noise-induced turbulence in nonlocally coupled oscillators. *Phys Rev E—Stat Nonlinear, Soft Matter Phys*. 2007; 75. <https://doi.org/10.1103/PhysRevE.75.036209> PMID: 17500771
13. Cross MC, Hohenberg PC. Pattern formation outside of equilibrium. *Rev Mod Phys*. 1993; 65: 851. <https://doi.org/10.1103/RevModPhys.65.851>
14. Kolmogorov NA. The local structure of turbulence in incompressible viscous fluid for very large Reynolds numbers. *C R Acad Sci URSS*. 1941; 30: 301–305. Available: <https://ci.nii.ac.jp/naid/20000584634>
15. Kolmogorov NA. Dissipation of energy in the locally isotropic turbulence. *C R Acad Sci URSS*. 1941; 32: 16–18. Available: <https://ci.nii.ac.jp/naid/10028205216>
16. Deco G, Kringelbach ML, Jirsa VK, Ritter P. The dynamics of resting fluctuations in the brain: metastability and its dynamical cortical core. *Sci Reports* 2017 71. 2017; 7: 1–14. <https://doi.org/10.1038/s41598-017-03073-5> PMID: 28596608
17. Saenger VM, Kahan J, Foltynie T, Friston K, Aziz TZ, Green AL, et al. Uncovering the underlying mechanisms and whole-brain dynamics of deep brain stimulation for Parkinson's disease. *Sci Reports* 2017 71. 2017; 7: 1–14. <https://doi.org/10.1038/s41598-017-10003-y> PMID: 28851996
18. Deco G, Cabral J, Saenger VM, Boly M, Tagliazucchi E, Laufs H, et al. Perturbation of whole-brain dynamics in silico reveals mechanistic differences between brain states. *Neuroimage*. 2018; 169: 46–56. <https://doi.org/10.1016/j.neuroimage.2017.12.009> PMID: 29225066
19. Jobst BM, Hindriks R, Laufs H, Tagliazucchi E, Hahn G, Ponce-Alvarez A, et al. Increased Stability and Breakdown of Brain Effective Connectivity During Slow-Wave Sleep: Mechanistic Insights from Whole-Brain Computational Modelling. *Sci Reports* 2017 71. 2017; 7: 1–16. <https://doi.org/10.1038/s41598-017-04522-x> PMID: 28680119
20. Messé A, Rudrauf D, Benali H, Marrelec G. Relating Structure and Function in the Human Brain: Relative Contributions of Anatomy, Stationary Dynamics, and Non-stationarities. *PLOS Comput Biol*. 2014; 10: e1003530. <https://doi.org/10.1371/journal.pcbi.1003530> PMID: 24651524
21. Ghosh A, Rho Y, McIntosh AR, Kötter R, Jirsa VK. Noise during rest enables the exploration of the brain's dynamic repertoire. *PLoS Comput Biol*. 2008; 4: e1000196. <https://doi.org/10.1371/journal.pcbi.1000196> PMID: 18846206
22. Deco G, Jirsa VK. Ongoing cortical activity at rest: Criticality, multistability, and ghost attractors. *J Neurosci*. 2012; 32: 3366–3375. <https://doi.org/10.1523/JNEUROSCI.2523-11.2012> PMID: 22399758
23. Hansen ECA, Battaglia D, Spiegler A, Deco G, Jirsa VK. Functional connectivity dynamics: Modeling the switching behavior of the resting state. *Neuroimage*. 2015; 105: 525–535. <https://doi.org/10.1016/j.neuroimage.2014.11.001> PMID: 25462790
24. Cabral J, Kringelbach ML, Deco G. Exploring the network dynamics underlying brain activity during rest. *Prog Neurobiol*. 2014; 114: 102–131. <https://doi.org/10.1016/j.pneurobio.2013.12.005> PMID: 24389385
25. Casali AG, Gosseries O, Rosanova M, Boly M, Sarasso S, Casali KR, et al. A Theoretically Based Index of Consciousness Independent of Sensory Processing and Behavior. *Sci Transl Med*. 2013; 5: 198ra105–198ra105. <https://doi.org/10.1126/scitranslmed.3006294> PMID: 23946194

26. Ferrarelli F, Massimini M, Sarasso S, Casali A, Riedner BA, Angelini G, et al. Breakdown in cortical effective connectivity during midazolam-induced loss of consciousness. *Proc Natl Acad Sci*. 2010; 107: 2681–2686. <https://doi.org/10.1073/pnas.0913008107> PMID: 20133802
27. Massimini M, Ferrarelli F, Huber R, Esser SK, Singh H, Tononi G. Breakdown of Cortical Effective Connectivity During Sleep. *Science* (80-). 2005; 309: 2228–2232. <https://doi.org/10.1126/science.1117256> PMID: 16195466
28. Tik M, Hoffmann A, Sladky R, Tomova L, Hummer A, Navarro de Lara L, et al. Towards understanding rTMS mechanism of action: Stimulation of the DLPFC causes network-specific increase in functional connectivity. *Neuroimage*. 2017; 162: 289–296. <https://doi.org/10.1016/j.neuroimage.2017.09.022> PMID: 28912081
29. Santarnecchi E, Momi D, Sprugnoli G, Neri F, Pascual-Leone A, Rossi A, et al. Modulation of network-to-network connectivity via spike-timing-dependent noninvasive brain stimulation. *Hum Brain Mapp*. 2018; 39: 4870–4883. <https://doi.org/10.1002/hbm.24329> PMID: 30113111
30. Kunze T, Hunold A, Haueisen J, Jirsa V, Spiegler A. Transcranial direct current stimulation changes resting state functional connectivity: A large-scale brain network modeling study. *Neuroimage*. 2016; 140: 174–187. <https://doi.org/10.1016/j.neuroimage.2016.02.015> PMID: 26883068
31. Deco G, Kringelbach ML, Arnatkeviciute A, Oldham S, Sabarodien K, Rogasch NC, et al. Dynamical consequences of regional heterogeneity in the brain's transcriptional landscape. *Sci Adv*. 2021; 7: eabf4752. <https://doi.org/10.1126/sciadv.abf4752> PMID: 34261652
32. Ipiña IP, Kehoe PD, Kringelbach M, Laufs H, Ibañez A, Deco G, et al. Modeling regional changes in dynamic stability during sleep and wakefulness. *Neuroimage*. 2020; 215: 116833. <https://doi.org/10.1016/j.neuroimage.2020.116833> PMID: 32289454
33. Daido H. Susceptibility of large populations of coupled oscillators. *Phys Rev E*. 2015; 91: 012925. <https://doi.org/10.1103/PhysRevE.91.012925> PMID: 25679699
34. Schartner MM, Pigorini A, Gibbs SA, Arnulfo G, Sarasso S, Barnett L, et al. Global and local complexity of intracranial EEG decreases during NREM sleep. *Neurosci Conscious*. 2017; 2017: 1–12. <https://doi.org/10.1093/nc/niw022> PMID: 30042832
35. Raichle ME, MacLeod AM, Snyder AZ, Powers WJ, Gusnard DA, Shulman GL. A default mode of brain function. *Proc Natl Acad Sci*. 2001; 98: 676–682. <https://doi.org/10.1073/pnas.98.2.676> PMID: 11209064
36. Hagmann P, Cammoun L, Gigandet X, Gerhard S, Ellen Grant P, Wedeen V, et al. MR connectomics: Principles and challenges. *J Neurosci Methods*. 2010; 194: 34–45. <https://doi.org/10.1016/j.jneumeth.2010.01.014> PMID: 20096730
37. Johansen-Berg H, Rushworth MFS. Using diffusion imaging to study human connective anatomy. *Annu Rev Neurosci*. 2009; 32: 75–94. <https://doi.org/10.1146/annurev.neuro.051508.135735> PMID: 19400718
38. Hagmann P, Kurlant M, Gigandet X, Thiran P, Wedeen VJ, Meuli R, et al. Mapping Human Whole-Brain Structural Networks with Diffusion MRI. *PLoS One*. 2007; 2: e597. <https://doi.org/10.1371/journal.pone.0000597> PMID: 17611629
39. Deco G, Cabral J, Woolrich MW, Stevner ABA, van Hartevelt TJ, Kringelbach ML. Single or multiple frequency generators in on-going brain activity: A mechanistic whole-brain model of empirical MEG data. *Neuroimage*. 2017; 152: 538–550. <https://doi.org/10.1016/j.neuroimage.2017.03.023> PMID: 28315461
40. Freyer F, Roberts JA, Ritter P, Breakspear M. A Canonical Model of Multistability and Scale-Invariance in Biological Systems. *PLoS Comput Biol*. 2012; 8: e1002634. <https://doi.org/10.1371/journal.pcbi.1002634> PMID: 22912567
41. Piccinini J, Ipiña IP, Laufs H, Kringelbach M, Deco G, Perl YS, et al. Noise-driven multistability vs deterministic chaos in phenomenological semi-empirical models of whole-brain activity. *Chaos An Interdiscip J Nonlinear Sci*. 2021; 31: 023127. <https://doi.org/10.1063/5.0025543> PMID: 33653038
42. Van Essen DC, Smith SM, Barch DM, Behrens TEJ, Yacoub E, Ugurbil K. The WU-Minn Human Connectome Project: An overview. *Neuroimage*. 2013; 80: 62–79. <https://doi.org/10.1016/j.neuroimage.2013.05.041> PMID: 23684880
43. Schaefer A, Kong R, Gordon EM, Laumann TO, Zuo X-N, Holmes AJ, et al. Local-Global Parcellation of the Human Cerebral Cortex from Intrinsic Functional Connectivity MRI. *Cereb Cortex*. 2018; 28: 3095–3114. <https://doi.org/10.1093/cercor/bhx179> PMID: 28981612
44. Perl YS, Pallavicini C, Ipiña IP, Demertzi A, Bonhomme V, Martial C, et al. Perturbations in dynamical models of whole-brain activity dissociate between the level and stability of consciousness. Taylor PN, editor. *PLoS Comput Biol*. 2021; 17: e1009139. <https://doi.org/10.1371/journal.pcbi.1009139> PMID: 34314430

45. Donnelly-Kehoe P, Saenger VM, Lisofsky N, Kühn S, Kringelbach ML, Schwarzbach J, et al. Reliable local dynamics in the brain across sessions are revealed by whole-brain modeling of resting state activity. *Hum Brain Mapp*. 2019; 40: 2967–2980. <https://doi.org/10.1002/hbm.24572> PMID: 30882961
46. Montbrío E, Blasius B. Using nonisochronicity to control synchronization in ensembles of nonidentical oscillators. *Chaos An Interdiscip J Nonlinear Sci*. 2003; 13: 291. <https://doi.org/10.1063/1.1525170> PMID: 12675436
47. Montbrío E, Pazó D. Shear diversity prevents collective synchronization. *Phys Rev Lett*. 2011; 106: 254101. <https://doi.org/10.1103/PhysRevLett.106.254101> PMID: 21770641
48. Ercsey-Ravasz M, Markov NT, Lamy C, VanEssen DC, Knoblauch K, Toroczkai Z, et al. A Predictive Network Model of Cerebral Cortical Connectivity Based on a Distance Rule. *Neuron*. 2013; 80: 184–197. <https://doi.org/10.1016/j.neuron.2013.07.036> PMID: 24094111
49. Wang Z, Bovik AC, Sheikh HR, Simoncelli EP. Image quality assessment: From error visibility to structural similarity. *IEEE Trans Image Process*. 2004; 13: 600–612. <https://doi.org/10.1109/tip.2003.819861> PMID: 15376593
50. Spiegler A, Hansen ECA, Bernard C, McIntosh AR, Jirsa VK. Selective Activation of Resting-State Networks following Focal Stimulation in a Connectome-Based Network Model of the Human Brain. *eNeuro*. 2016; 3. <https://doi.org/10.1523/ENEURO.0068-16.2016> PMID: 27752540
51. Deco G, Jirsa VK, McIntosh AR. Resting brains never rest: Computational insights into potential cognitive architectures. *Trends Neurosci*. 2013; 36: 268–274. <https://doi.org/10.1016/j.tins.2013.03.001> PMID: 23561718
52. Bose I, Ghosh S. Bifurcation and criticality. *J Stat Mech Theory Exp*. 2019; 2019: 043403. <https://doi.org/10.1088/1742-5468/AB11D8>
53. Chialvo DR. Emergent complex neural dynamics. *Nat Phys* 2010 610. 2010; 6: 744–750. <https://doi.org/10.1038/nphys1803>
54. Cocchi L, Gollo LL, Zalesky A, Breakspear M. Criticality in the brain: A synthesis of neurobiology, models and cognition. *Prog Neurobiol*. 2017; 158: 132–152. <https://doi.org/10.1016/j.pneurobio.2017.07.002> PMID: 28734836
55. Deco G, Cruzat J, Cabral J, Tagliazucchi E, Laufs H, Logothetis NK, et al. Awakening: Predicting external stimulation to force transitions between different brain states. *Proc Natl Acad Sci U S A*. 2019; 116: 18088–18097. <https://doi.org/10.1073/pnas.1905534116> PMID: 31427539
56. Spiegler A, Abadchi JK, Mohajerani M, Jirsa VK. In silico exploration of mouse brain dynamics by focal stimulation reflects the organization of functional networks and sensory processing. *Netw Neurosci*. 2020; 4: 807–851. [https://doi.org/10.1162/netn\\_a\\_00152](https://doi.org/10.1162/netn_a_00152) PMID: 33615092
57. Rosanova M, Gosseries O, Casarotto S, Boly M, Casali AG, Bruno MA, et al. Recovery of cortical effective connectivity and recovery of consciousness in vegetative patients. *Brain*. 2012; 135: 1308–1320. <https://doi.org/10.1093/brain/awr340> PMID: 22226806
58. Hawrylycz MJ, Lein ES, Guillozet-Bongaarts AL, Shen EH, Ng L, Miller JA, et al. An anatomically comprehensive atlas of the adult human brain transcriptome. *Nature*. 2012; 489: 391–399. <https://doi.org/10.1038/nature11405> PMID: 22996553
59. Arnatkeviciute A, Fulcher BD, Fornito A. A practical guide to linking brain-wide gene expression and neuroimaging data. *Neuroimage*. 2019; 189: 353–367. <https://doi.org/10.1016/j.neuroimage.2019.01.011> PMID: 30648605
60. Kringelbach ML, Cruzat J, Cabral J, Knudsen GM, Carhart-Harris R, Whybrow PC, et al. Dynamic coupling of whole-brain neuronal and neurotransmitter systems. *Proc Natl Acad Sci*. 2020; 117: 9566–9576. <https://doi.org/10.1073/pnas.1921475117> PMID: 32284420
61. Fox MD, Buckner R, White MP, Greicius MD, Pascual-Leone A. Efficacy of transcranial magnetic stimulation targets for depression is related to intrinsic functional connectivity with the subgenual cingulate. *Biol Psychiatry*. 2012; 72: 595–603. <https://doi.org/10.1016/j.biopsych.2012.04.028> PMID: 22658708
62. Kringelbach ML, Jenkinson N, Owen SLF, Aziz TZ. Translational principles of deep brain stimulation. *Nat Rev Neurosci* 2007 88. 2007; 8: 623–635. <https://doi.org/10.1038/nrn2196> PMID: 17637800
63. Dayan E, Censor N, Buch ER, Sandrini M, Cohen LG. Noninvasive brain stimulation: from physiology to network dynamics and back. *Nat Neurosci* 2013 167. 2013; 16: 838–844. <https://doi.org/10.1038/nn.3422> PMID: 23799477
64. Yeo BTT, Krienen FM, Sepulcre J, Sabuncu MR, Lashkari D, Hollinshead M, et al. The organization of the human cerebral cortex estimated by intrinsic functional connectivity. *J Neurophysiol*. 2011; 106: 1125–1165. <https://doi.org/10.1152/jn.00338.2011> PMID: 21653723
65. Yang Y, Qiao S, Sani OG, Sedillo JI, Ferentino B, Pesaran B, et al. Modelling and prediction of the dynamic responses of large-scale brain networks during direct electrical stimulation. *Nat Biomed Eng* 2021 54. 2021; 5: 324–345. <https://doi.org/10.1038/s41551-020-00666-w> PMID: 33526909

66. Honey CJ, Sporns O, Cammoun L, Gigandet X, Thiran JP, Meuli R, et al. Predicting human resting-state functional connectivity from structural connectivity. *Proc Natl Acad Sci U S A*. 2009; 106: 2035–2040. <https://doi.org/10.1073/pnas.0811168106> PMID: 19188601
67. Breakspear M. Dynamic models of large-scale brain activity. *Nat Neurosci*. 2017; 20: 340–352. <https://doi.org/10.1038/nn.4497> PMID: 28230845
68. Jirsa VK, Jantzen KJ, Fuchs A, Kelso JAS. Spatiotemporal forward solution of the EEG and MEG using network modeling. *IEEE Trans Med Imaging*. 2002; 21: 493–504. <https://doi.org/10.1109/TMI.2002.1009385> PMID: 12071620
69. Kringelbach ML, Deco G. Brain States and Transitions: Insights from Computational Neuroscience. *Cell Rep*. 2020; 32: 108128. <https://doi.org/10.1016/j.celrep.2020.108128> PMID: 32905760
70. Angelakis E, Liouta E, Andreadis N, Korfiatis S, Ktonas P, Stranjalis G, et al. Transcranial Direct Current Stimulation Effects in Disorders of Consciousness. *Arch Phys Med Rehabil*. 2014; 95: 283–289. <https://doi.org/10.1016/j.apmr.2013.09.002> PMID: 24035769
71. Zhang Y, Song W. Transcranial direct current stimulation in disorders of consciousness: a review. 2017; 128: 255–261. <https://doi.org/10.1080/00207454.2017.1381094> PMID: 28918680
72. Ozdemir RA, Tadayon E, Boucher P, Momi D, Karakhanyan KA, Fox MD, et al. Individualized perturbation of the human connectome reveals reproducible biomarkers of network dynamics relevant to cognition. *Proc Natl Acad Sci U S A*. 2020; 117: 8115–8125. <https://doi.org/10.1073/pnas.1911240117> PMID: 32193345
73. Deco G, McIntosh AR, Shen K, Hutchison RM, Menon RS, Everling S, et al. Identification of Optimal Structural Connectivity Using Functional Connectivity and Neural Modeling. *J Neurosci*. 2014; 34: 7910–7916. <https://doi.org/10.1523/JNEUROSCI.4423-13.2014> PMID: 24899713
74. Shen K, Bezgin G, Schirner M, Ritter P, Everling S, McIntosh AR. A macaque connectome for large-scale network simulations in TheVirtualBrain. *Sci Data* 2019 61. 2019; 6: 1–12. <https://doi.org/10.1038/s41597-019-0129-z> PMID: 31316116
75. Ponce-Alvarez A, Uhrig L, Deco N, Signorelli CM, Kringelbach ML, Jarraya B, et al. Macroscopic quantities of collective brain activity during wakefulness and anesthesia. *bioRxiv*. 2021; 2021.02.03.429578. <https://doi.org/10.1101/2021.02.03.429578>
76. Barttfeld P, Uhriga L, Sitta JD, Sigmane M, Jarraya B, Dehaene S. Signature of consciousness in the dynamics of resting-state brain activity. *Proc Natl Acad Sci U S A*. 2015; 112: 887–892. <https://doi.org/10.1073/pnas.1418031112> PMID: 25561541
77. Desikan RS, Ségonne F, Fischl B, Quinn BT, Dickerson BC, Blacker D, et al. An automated labeling system for subdividing the human cerebral cortex on MRI scans into gyral based regions of interest. *Neuroimage*. 2006; 31: 968–980. <https://doi.org/10.1016/j.neuroimage.2006.01.021> PMID: 16530430
78. Smith SM, Beckmann CF, Andersson J, Auerbach EJ, Bijsterbosch J, Douaud G, et al. Resting-state fMRI in the Human Connectome Project. *Neuroimage*. 2013; 80: 144–168. <https://doi.org/10.1016/j.neuroimage.2013.05.039> PMID: 23702415
79. Schröder TN, Haak K V., Jimenez NIZ, Beckmann CF, Doeller CF. Functional topography of the human entorhinal cortex. *Elife*. 2015; 4: 1–17. <https://doi.org/10.7554/ELIFE.06738> PMID: 26052748
80. Griffanti L, Salimi-Khorshidi G, Beckmann CF, Auerbach EJ, Douaud G, Sexton CE, et al. ICA-based artefact removal and accelerated fMRI acquisition for improved resting state network imaging. *Neuroimage*. 2014; 95: 232–247. <https://doi.org/10.1016/j.neuroimage.2014.03.034> PMID: 24657355
81. Oostenveld R, Fries P, Maris E, Schoffelen JM. FieldTrip: Open source software for advanced analysis of MEG, EEG, and invasive electrophysiological data. *Comput Intell Neurosci*. 2011; 2011. <https://doi.org/10.1155/2011/156869> PMID: 21253357
82. Cordes D, Haughton VM, Arfanakis K, Carew JD, Turski PA, Moritz CH, et al. Frequencies Contributing to Functional Connectivity in the Cerebral Cortex in “Resting-state” Data. *Am J Neuroradiol*. 2001; 22. PMID: 11498421
83. Horn A, Blankenburg F. Toward a standardized structural–functional group connectome in MNI space. *Neuroimage*. 2016; 124: 310–322. <https://doi.org/10.1016/j.neuroimage.2015.08.048> PMID: 26327244
84. Horn A, Neumann WJ, Degen K, Schneider GH, Kühn AA. Toward an electrophysiological “Sweet spot” for deep brain stimulation in the subthalamic nucleus. *Hum Brain Mapp*. 2017; 38: 3377–3390. <https://doi.org/10.1002/hbm.23594> PMID: 28390148
85. Lempel A, Ziv J. On the Complexity of Finite Sequences. *IEEE Trans Inf Theory*. 1976; 22: 75–81. <https://doi.org/10.1109/TIT.1976.1055501>
86. Burt JB, Demirtaş M, Eckner WJ, Navejar NM, Ji JL, Martin WJ, et al. Hierarchy of transcriptomic specialization across human cortex captured by structural neuroimaging topography. *Nat Neurosci*. 2018; 21: 1251–1259. <https://doi.org/10.1038/s41593-018-0195-0> PMID: 30082915